On the shear failure of incipient rock discontinuities under CNL and CNS boundary conditions: Insights from DEM modelling

J Shang[1], Z Zhao[1], S Ma[2]

[1]Nanyang Centre for Underground Space, School of Civil and Environmental Engineering, Nanyang Technological University, Singapore.

[2] Department of Civil and Environmental Engineering, Colorado School of Mines, USA.

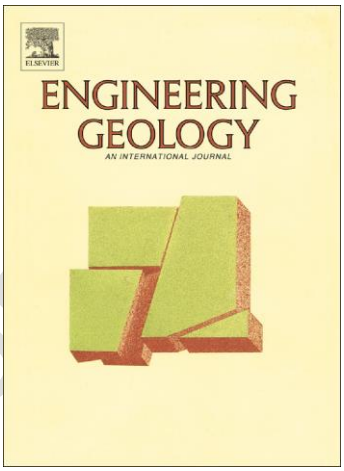

Received date: 14 Aug 2017
Revised date: 13 Jan 2018
Accepted date: 17 Jan 2018

https://doi.org/10.1016/j.enggeo.2018.01.012

Abstract

This paper presents a numerical investigation of the effects of boundary conditions, i.e., constant normal load (CNL) and constant normal stiffness (CNS), on the failure mechanism of incipient rock discontinuities in direct shear. A series of numerical simulations were performed using the particle-based discrete element method (DEM), in which rock matrix and rock bridges (on incipient joint planes) were modeled as an assembly of rigid particles that were bonded together at their contacts. Smooth-joint model was assigned to particles of the persistent portions of incipient rock joints. Input micro-parameters of particles, bonds and smooth-joint

were calibrated against a series of laboratory experiments. The study reveals that CNL and CNS boundary conditions significantly affect shear characteristics of incipient rock discontinuities. Peak shear stress increased significantly (up to three times) in the CNS direct shear in comparison with that measured in the CNL direct shear under the same initially applied normal stresses. The significant increase of shear stress in the CNS direct shear tests conducted in this study was related to the opening of newly created micro-cracks and creation of the rupture zones within the rock bridges, leading to a dramatic increase in the normal stresses. In the meanwhile, yield behavior was observed in the CNS direct shear while brittle failure was noticed in the CNL direct shear. It is also found that micro-cracks initiated at the vicinity of rock bridges in both CNL and CNS shear tests, while they propagated differently due to the gradual increase of normal stress under CNS boundary conditions.

Keywords: Incipient rock discontinuity; persistence; rock bridge; direct shear; boundary conditions; discrete element method

1. Introduction

Translational rockslides and instability of rock masses can be associated with the shear failure of incipient rock discontinuities. The failure is a combination of sliding along persistent discontinuity sections and rupturing of intervening incipient portions (often represented by rock bridges) (Einstein et al.,1983; Stead and Wolter, 2015; Tannant et al., 2017). Incipient rock discontinuities herein refer to rock joints [1] that are not fully developed with geological time; they therefore retain considerable shear and tensile strength sometimes even approaching that of parent rock (Shang et al., 2015 and 2016). (Footer of this page: [1] Rock joints are often used essentially

synonymously with rock discontinuities in published literature [e.g. Hencher and Richard, 2015] and that practice was adopted in this study.)

It has been understood that asperities and texture (Hencher and Richard, 2015; Bahaaddini et al., 2016), geometry and strength of rock bridges (Kemeny, 2005), roughness (Hencher and Richard, 2015) and water conditions (Kim and Inoue, 2003) can influence the shear strength of incipient rock discontinuities. Apart from these factors, the shear failure mechanism is also influenced by boundary conditions. Constant normal load (CNL) and constant normal stiffness (CNS) boundary conditions both exist in nature (Gischig et al., 2011 and 2011a; Poturovic et al., 2015). Figure 1 shows a rock slope with many irregular rock blocks and incipient rock joints. These incipient rock joints may fail in shear under CNL boundary condition, threatening vehicles on the high way. Figure 2 presents a schematic diagram showing CNL and CNS boundary conditions. A translational rockslide may occur due to the shear failure of incipient rock joints under the CNL condition (Case A). Normal load, N, (mainly arising from self-weight, W) remains constant and rock (in grey) overlaying the shear plane can dilate freely during shear. For cases where unstable blocks are away from free surfaces, either confined by un-tensional rock bolts (Nemcik et al. 2014) (e.g., Case B in Figure 2) or surrounding rocks in the underground (e.g., Case C in Figure 2), dilatant deformation are resisted during shear. This will lead to an increase of normal (i.e. confining) stress. Increased normal stress, in this sense, will conversely enhance the shear strength of rock discontinuities (Indraratna and Haque, 2000). This phenomenon in nature can be represented by CNS boundary condition (Shrivastava and Rao, 2013; Bewick et al., 2014).

Shear failure of rock discontinuities under CNL boundary conditions has been widely investigated in the laboratory (e.g. Hencher, 1976; Bandis et al., 1981; Gehle and Kutter, 2003) and through numerical modelling (e.g. Zhang et al., 2006; Shrivastava and Rao, 2010; Bahaaddini et al., 2016). Among these investigations authors focused on the mechanical (opened) rock joints that are, to some extent, special cases of incipient ones (Shang et al. 2015; Shang 2016). Attempts have been undertaken to study the shear strength of incipient rock discontinuities. Lajtai (1969) found that direct shear strength of a coplanar incipient rock joint depends on rock bridge strength and joint friction using replica samples. Rock bridges may fail in forms of tension and shear depending on the normal and shear stress conditions. Similar replica rock joints were prepared by other researchers such as Savilahti et al. (1990) who found that rock bridge generally failed in tension. Gehle and Kutter (2003), in their study of breakage and shear failure of rock joints, found that crack initiated by the formation of wing cracks and propagated into rock bridges. Note that joints in their study were not parallel to the shear direction. A further study was presented by Zhang et al. (2006) based on software rock failure process analysis (RFPA 2D), in which more geometrical parameters of rock joints were involved. They found that the propagation of wing cracks depended on the joint separation and its relative orientation to the shear direction.

Due to the difficulty of experimentation, only a few experimental investigations were reported on CNS direct shear. Indararatna and Haque (1997) investigated the influence of bentonite infill on the shear behavior of soft joints deformed under CNS conditions. One main conclusion from that study is that the peak shear strength of filled rock joints approached that of infill when the ratio of infill thickness to asperity height reached 1.6. Shrivastava and Rao (2013) developed a large-scale direct

shear test machine in the laboratory, in which varying normal stress was generated by a hydraulic servo-valve to represent CNS boundary conditions. Poturovic et al. (2015) provided some insights into the shear failure of artificial rock joints deformed under CNL and CNS conditions. They found that dilation potential depended on the external boundary conditions and stiffness. Apart from these laboratory investigations, a series of analytical models have been proposed to study CNS shear behavior of rock joints, including those of Saeb and Amadei (1990), Indraratna and Haque (2000) and Lee et al. (2014), see Thirukumaran and Indraratna (2016) for a brief review in this regard. For numerical modelling of CNS shear of rock discontinuities, few literatures are available. Indraratna and Haque (2000) examined the shear behavior of soft saw-tooth rock joints under CNS conditions using Universal Distinct Element Code (UDEC).

The literatures aforementioned mainly focused on the shear behavior of mechanical rock discontinuities. It is rare to see direct shear tests on incipient rock joints. As stated earlier, the presence of rock bridges can give a high strength reserve, which should be considered in practical situations. To fortify the literature in this area, this study presents an investigation of the shear failure of incipient rock discontinuities using the particle-based discrete element method (DEM), with a primary aim of investigating the influence of boundary conditions (i.e., CNL and CNS). The particle flow code (Cundall and Strack, 1979) has been widely employed in the modelling of rock and discontinuities (Zhang and Thornton, 2007; Bewick et al., 2014; Duan and Kwok, 2016; Mehranpour and Kulatilake, 2017; Shang et al. 2017a) and this code was used in this study.

2. Methodology of modelling

2.1 DEM model and calibration

In the study, a DEM model was established using the particle flow code 3D (PFC3D) produced by the Itasca Consulting Group. In the model, rock matrix and rock bridge were represented as an assembly that were parallel bounded at their contacts. The bond will break in either shear or tension when external load exceeds the bond strength (Itasca Consulting Group Inc 2008). Persistent joint sections were simulated by the smooth-joint model (SJM) developed by Cundall (2000).

The parallel-bonded DEM model was calibrated against uniaxial compression test on intact Horton Formation Siltstone. In the experiment, cylindrical samples having a height to diameter ratio of 2.4 were prepared and ends of samples were ground flat according to the ISRM standard (Fairhurst and Hudson 1999). The prepared samples were compressed with a uniform loading rate of 0.5 MPa/s using a servo-controlled loading machine (MAND). Normal load and axial and lateral strain were recorded during the test. Figure 3a shows two representative curves of axial stress against axial and lateral strains. The stress-strain curves were used in the calibration and the procedure was similar to that used by Bahaaddini et al. (2013). In the calibration, a DEM sample containing 9596 particles with a radius ranging between 1.0 and 1.5 mm was generated. The size of the DEM sample (120 mm × 50 mm) was the same as that of samples used in laboratory experiment. Modulus of particles and parallel bond was firstly calibrated through a trial-and-error process, followed by the calibration of normal to shear stiffness ratio. After that, the bond cohesion, tensile strength and friction angle were varied to match the uniaxial compressive strength. Figure 3a shows a comparison of the calibrated numerical and laboratory results. As can be seen in Figure 3a, a good agreement was reached. Corresponding calibrated micro-parameters are listed in Table 1.

150 The calibration of SJM in this study involved the micro-parameters selection of
151 smooth joint normal stiffness, shear stiffness and friction coefficient. Smooth joint
152 normal stiffness was calibrated against normal deformability test; and shear stiffness
153 and friction coefficient were calibrated against direct shear test. In the experimental
154 normal deformability test, intact cylindrical samples (70 mm in diameter and 150 mm
155 in length) and identical samples with a horizontal planar joint were prepared (Shang
156 2016; ASTM 2014). Again, two ends of samples were ground flat. Prepared samples
157 were uniaxially compressed to approximately half of UCS of intact rock at a constant
158 loading rate of 0.5 MPa/s. Normal force and normal deformation of intact rock and
159 rock with a horizontal joint were recorded during loading. Joint normal deformation
160 was estimated by subtracting intact rock normal deformation from normal
161 deformation of intact rock with a joint (Bandis et al. 1983). A representative result of
162 stress and joint normal displacement curve is shown in Figure 3b. As it can be seen,
163 the curve contains a non-linear part (mainly due to the closure of joint) and an
164 approximately linear part (due to the compression of intact rock). Calibration of the
165 smooth joint normal stiffness was conducted on a DEM cylindrical sample (with the
166 same dimension as the physical samples) containing a horizontal joint plane
167 (represented by SJM). The particle size followed a uniform distribution with R_{min}=1.0
168 mm and R_{max}/R_{min}=1.5 (Shang et al. 2017a). The constructed DEM sample was
169 compressed continuously with a constant loading rate of 0.005 m/s. Test was
170 terminated when normal stress reached approximately half of UCS of intact rock.
171 Normal stress and normal displacement were recorded during loading. Smooth joint
172 normal stiffness was varied to match the experimental result, i.e., the curve of axial
173 stress and joint normal displacement as illustrated in Figure 3b. Corresponding
174 micro-parameter is listed in Table 1.

To calibrate smooth joint shear stiffness and friction coefficient, direct shear tests on a Horton Formation Siltstone joint were performed using a Robertson Shear Box (developed by Professor Evert Hoek). A constant normal stress of 2 MPa was applied on the jointed sample using an equipped hand jack. The normal and shear loads were recorded by Bourdon tube load gauges and shear displacement was logged by a dial gauge. Shear test was terminated when horizontal shear displacement reached 10 mm. Shear stresses under a normal stress of 2 MPa and corresponding horizontal displacement are plotted in Figure 3c. It should be noted that the authors have attempted to conduct direct shear tests under higher normal stresses (i.e., 4 and 6 MPa) using the Robertson Shear Box, but they failed in their attempts to get reliable data due to the intrinsic limitations of the Robertson Shear Box (see discussion of this point in section 5).

Following the procedures of Bahaaddini et al. (2013), smooth joint shear stiffness was firstly varied to match the shear stiffness of the planar joint under a normal stress of 2 MPa, followed by varying the smooth joint friction coefficient to match the peak shear strength. Figure 3c shows a comparison of the numerical and laboratory results. As shown in Figure 3c, a good agreement was reached. Corresponding calibrated micro-parameters are list in Table 1. To understand the shear characteristics of the DEM model under higher normal stresses, additional two DEM simulations under normal stresses of 4 and 6 MPa were performed using the parameters listed in Table 1. Numerical results are shown in Figure 3c (red and black lines). It can be seen that the friction angles are approximately the same under different normal stresses (around 31°) and the cohesion is approximately zero (as a mechanical joint was tested).

2.2 DEM Model setup of CNL and CNS direct shear tests

Figure 4 shows the model setup of direct shear tests under CNL and CNS boundary conditions. In the CNL shear model (Figure 4a), a shear box with a dimension of 100 mm (length) x 100 mm (width) x 40 mm (height) was created. Rock sample comprised around 49000 particles with minimum radius of 1.0 mm and a ratio of maximum to minimum particle radius (R_{max} / R_{min}) of 1.5, which follows a normal distribution (Potyondy and Cundall, 2004; Shang et al. 2017a). An incipient rock joint oriented parallel to the shear direction was created, as shown in Figure 4c (particles forming rock matrix are not shown for clarity). The rock bridge area along the incipient joint plane was closed by black dashed lines. The lower shear box was fixed (purple in Figure 4c) and the upper box was deformed (red in Figure 4c) at a constant shear velocity of 0.02 m/s. To ensure CNL boundary condition, normal stresses with magnitudes of 6, 20 and 40 MPa were applied on the top shear box respectively and kept constant using the servo mechanism (Itasca Consulting Group Inc 2008). The mean shear stress was calculated by dividing the reaction forces acting along the two side walls of the top box by the area of incipient joint plane.

The CNS direct shear test was set up based on the CNL shear model which is similar to that used by Bewick et al. (2014). Unlike the free boundary constraint for CNL shear (Figure 4a), an additional cap of material with a depth of 20 mm was generated on the top of the upper shear box (grey particles in Figure 4b) to prevent dilatant deformation during shear deformation. The material comprised particles that were bonded together at their contacts and the bonds between them are non-breakable. Stiffness of the cap material was assigned by modulus of the particles and bonds. Three different modulus values (i.e., 1, 10 and 30 GPa, respectively) were studied.

To generate the cap material, five additional walls (aw1-aw5, see Figure 4d) were created on the top of the upper shear box. It is noted that only one horizontal interface wall was created between the cap material and the upper shear box and both sides of the wall were active in the simulation model (Figure 4d). After the wall generation, assemblies of particles (with the same particle size distribution as that used in the CNL shear, Figure 4a) were generated and the cap and the shear box were filled by the particles separately. After model reached the static equilibrium, the particles contacting the horizontal interface wall were detected which can be divided into two groups. The first group comprised the particles above the interface wall (red particles in Figure 4b) and the second group involved the particles below the interface wall (green particles in Figure 4b). The horizontal interface wall between the cap and the upper shear box was then deleted (Figure 4d). Cycling continued until static equilibrium was achieved. New contacts between the red and green particles were generated in that process and linear model without contact bond and friction was applied at the newly generated contacts. The frictionless linear model applied between the cap material and the upper shear box guaranteed that there was no shear force at their interface during the simulation; and the cap material only provided normal resistance to the dilatant deformation of the upper shear box, thereby mimicking the CNS boundary condition.

In the CNS direct shear, the upper shear box and the cap were fixed whilst the lower shear box was deformed (see Figure 4d). Normal stresses with magnitudes of 6, 20 and 40 MPa were applied on the top wall (i.e., aw5, Figure 4d), respectively; and the wall was fixed after the initial applied normal stresses were achieved using the servo mechanism (Itasca Consulting Group Inc 2008). Similarly, the mean shear stress was calculated by dividing the reaction forces acting along two the side walls of the

lower box by the area of the incipient joint plane. The normal stress was calculated by dividing the reaction force acting on the top wall of the cap by the area of the wall. Fifteen measurement spheres were arranged in the rock bridge area to monitor local stresses during the test (Figure 4d).

3. DEM modelling results

3.1 Shear stress and strain characteristics

A series of CNL and CNS direct shear tests were conducted using the carlibrated DEM model and the numerical simulation scheme described in section 2.2. Figure 5 shows the integrated shear stress and strain curves of CNL direct shear under different normal stresses (6, 20 and 40 MPa) and CNS direct shear under different magnitudes of normal stiffness (represented by different modulus of cap material, i.e., 1, 10 and 30 GPa, respectively). It can be seen that the shear strengths measured in CNS direct shear were much larger compared with that measured in CNL shear. The stress-strain curves in the CNS shear were similar to one another (Figure 5a) and an early shear strength (less shear strain) occurred for the case with a smaller confinement stiffness (i.e. 1 GPa). Furthermore, the stress paths were quite similar for other two series of tests when initially applied normal stresses (lANS) were 20 and 40 MPa.

As anticipated, for CNS direct shear under the same initial normal stress, peak shear stress increased with the increase of the modulus of the cap material. For example in Figure 5a, the peak shear stress was 52.2 MPa when modulus of cap material was 1 GPa, while it increased up to 64.1 MPa when modulus was 30 GPa. The stress-strain curves in CNS shear exhibited a clear yield behavior (Yield points are indicated by circles in Figures 5a, 5b and 5c). Prior to the yield stage, elastic

behavior dominated, during which stress oscillations (see the close-up view in Figure 5a) were observed due to the fracturing of rock bridges (break of bonds between particles). Followed by the yield deformation, for all simulations, shear strengths reached within a shear strain of approximately 0.015.

Compared with the CNS direct shear, on the contrary, stress-strain curves of CNL shear exhibited a same yield and peak strength (see Figure 5a). Tangent modulus of the curves (in the elastic deformation stage) prior to the yield points were smaller in comparison to that measured in CNS direct shear.

Stiffness of confinement and initially applied normal stress in CNS direct shear can influence the shear strength and failure mechanism (Bewick et al., 2014). Figure 6 shows relative stress increases corresponding to the yield and peak points when modulus of cap material increased from 1 to 30 GPa. It is observed that the increment of stresses at the yield and peak points decreased slightly when the initially applied normal stress was increased. The relative increase of peak shear stress was 0.179 for a cap modulus of 10 GPa when initially applied normal stress was 6 MPa, it dropped to 0.127 when initially applied normal stress was 40 MPa (Figure 6).

3.2 Shear stress versus normal stress in CNS direct shear

Figure 7 shows the relationship between shear stress and normal stress in CNS direct shear. Significant increase of normal stress was measured which was related to shear rupture of the rock bridge within the tested incipient joint plane and was not a result of shearing on pre-existing asperities (persistent joint sections are represented by smooth-joint model in this study).

296 In Figure 7a, shear stress curves followed a similar path until the first yield point
297 (51.2 MPa) was reached (cap modulus was 1 GPa). A much higher yield stress (59.3
298 MPa) was measured with a higher normal stress (22.5 MPa) when cap modulus was
299 10 GPa, followed by the appearance of peak shear stress (60 MPa) and then steady
300 reduction to around frictional strength (black dashed line in Figure 7a). A similar
301 trend was also observed for the case when cap modulus was 30 GPa (blue line in
302 Figure 7a). Linear coulomb strength envelop (dashed orange line) intersects stress
303 paths which demonstrates that this rule cannot be used to predict peak shear
304 strength under CNS boundary conditions because the peak stress under this
305 condition also depended on the stiffness of confinement (Bewick et al. 2014).
306 Likewise, at higher initially applied normal stresses (20 and 40 MPa), peak shear
307 strength reached with a larger normal stress when cap modulus was increased
308 (Figures 7b and 7c). Figure 8 shows peak normal stress against cap modulus under
309 CNS direct shear. It is observed that peak shear stresses measured were
310 proportional to the cap modulus and IANS. Note that zero cap modulus represents
311 the CNL boundary condition.

312 3.3 Micromechanical behavior: Stress versus evolution of micro-cracks

313 Figures 9, 10 and 11 show examples of stress characteristics under CNL shear and
314 CNS shear with cap modulus of 1 GPa and 30 GPa. Evolution of micro-cracks for
315 each test is graphically presented (Figures 9d, 10e and 11e). For visualization
316 purpose, a set of distinct colors were assigned to shear boxes and micro-cracks.
317 Shear boxes shown in red deformed (along the positive x-direction at a shear rate of
318 0.02 m/s) and those shown in purple stationed. Induced shear cracks were shown in
319 red and tensile cracks in yellow. For clarity, top and front walls are not shown; shear

planes (including persistent joint planes and rock bridges in between) and particles (forming the rock matrix) in the bottom shear box are shown.

In the example of CNL direct shear (Figure 9), shear stress, normal displacement and cumulative number of micro-cracks are plotted against shear strain (Figures 9a, 9b and 9c). Figure 9d shows the corresponding images monitored at five key stages shown in Figure 9c, i.e., test initiation (Point A), fracture initiation around tips of rock bridge (Point B), crack propagation (Point C), crack coalescence (Point D) and end of test run (Point E). It can be observed that cracks initiated around two edges of rock bridges at the shear strain of around 0.0028 and concentrated along the shear direction (Magenta dashed boxes in Figure 9dB). Then, cracks propagated in a clear trend, showing more concentration in the center of rock bridge area (indicated by the blue arrows in Figure 9dC). Peak shear stress reached at the Point D, at which micro-cracks coalesced in the middle, leaving two U-shaped areas of rock bridges (Figure 9dD). Peak shear stress reached (Figure 9a), accompanied by a significant increase of normal displacement (Figure 9b) and occurrence of more micro-cracks (Figure 9c). Note that the increase of normal displacement in the CNL direct shear was related to the servo-controlled mechanism for maintaining the required normal stress (6 MPa for this case) rather than dilation. Subsequently, shear stress dropped abruptly from the peak (21 MPa) to around 13 MPa, after which point no significant increase of the number of micro-cracks was observed. Figure 9dE shows the image at the end of the test run, in which some scattered microcracks were found around the edges of top shear box due to stress concentration.

In the CNS direct shear tests with a cap modulus of 1 GPa (Figure 10), fifteen shear stress paths were monitored through the test run using the measurement spheres described in Figure 4d. For clarity, they are plotted separately against shear strain

(Figures 10a and 10b). Unlike the CNL shear, the bottom shear box (red) deformed whilst the top shear box and the cap material stationed (in purple) (Figure 10eA). Micro-crack evolution, at the five stages described above, in the CNS direct shear (Figure 10e) exhibited a clear different pattern in comparison to that observed in the CNL direct shear (Figure 9d). Prior to appearance of the shear strength at Point D (Figures 10d and 10eD), micro-cracks initiated around two edges of rock bridges (Magenta dashed boxes in Figure 10eB) but propagated with an I-shaped pattern (indicated by blue arrows in Figure 10eC) towards the middle area of the rock bridge. At this stage, apart from the micro-cracks generated in the rock bridge, a small amount of micro-cracks were induced above the persistent joint surfaces (indicated by the blue dashed circles in Figure 10eC). The monitored shear stress paths at this particular stage exhibited clear peaks (Figures 10a and 10b), subsequently rise with oscillations, which was related to the opening of newly generated cracks and generation of rupture zone in the rock bridge area.

At the Point D, peak shear stress reached with the mirco-cracks approximately coalesced (Figure 10eD). Steady increase of the number of micro-cracks was still observed due to the break of bonds within the rock matrix (which is related to the highly increased normal stress and confinement in CNS direct shear). The increase of normal stress approached to a constant (just below 27.5 MPa) at the end of test run when no significant increase of the number of micro-cracks appeared on the shear plane (Figure 10eE). It can be noted that the relative increase of the number of shear micro-cracks (92%) in CNS and CNL was much larger than that for tensile micro-cracks (23%), which was due to the increment of normal stress in CNS shear, leading to more shear cracks.

An example of CNS direct shear with a higher cap modulus of 30 GPa is shown in Figure 11. The fracturing process was very different compared with that observed in the case with a smaller stiffness of confinement (1 GPa, Figure 10). Again, cracks initiated around two edges of rock bridges but with an early appearance of micro-cracks outside areas of the shear plane (Figure 11eB). Instead of the I-shaped pattern (Figure 10eC), micro-crack propagation led to a U-shaped area of rock bridge in the middle (blue arrows in Figure 11eC) and the rock bridge then disappeared gradually until the Point D. Peak shear stress reached at the Point D and reduced gradually with some oscillations until the end of test run. Another observation is that a large number of micro-cracks, especially shear micro-cracks (red), were created above the shear plane (Figures 11eD and 11eE) due to the significant increase of normal stress (up to 120 MPa in Figure 11a). The number of shear micro-cracks was 27047, which was around 5.7 times of that of tensile micro-cracks (4738).

Figures 12 shows contoured plots of micro-cracks induced in the CNL and CNS direct shear tests in which normal stress and IANS are both 6 MPa. Micro-cracks are plotted as poles on equal angle stereonets and they are not shown for clarity. Contoured areas are filled by red for CNL tests and by monochrome for CNS tests. Values in each legend represent the percentage of density of poles per 1% area. Rose diagrams showing the trends of micro-cracks in CNS direct shear and best-fit planes of poles are included. As illustrated in Figure 12, cracks orientated very differently for CNL and CNS direct shear, while for the series of CNS direct shear tests conducted under different confinement stiffness, orientation of induced micro-cracks exhibited a similar pattern. As seen from the rose diagrams, shear micro-cracks trended mainly between approximately 0 degree and 180 degree from north,

whereas tensile micro-cracks approximately between 180 degree and 360 degree from north (CNS tests in Figure 12). This finding also applies to other series of shear tests conducted in this study with a higher normal stress (for example 20 MPa in CNL shear) and IANS (for example 40 MPa in CNS shear) (Figures 13 and 14). It is also found that the magnitude of initially applied normal stress in CNS shear tests had some influence on the orientation and concentration of micro-cracks. For example, in the CNS shear tests under the same confinement stiffness of 10 GPa, density of shear micro-cracks ranged between 1% and 3% per 1% area when IANS was 6 MPa (see the first figure at the third row in Figure 12). While it reduced within 2% per 1% area when IANS was increased to 20 MPa (see the first figure at the third row in Figure 13). The number of micro-cracks increased with the increase of peak normal stress, irrespective of boundary conditions, as illustrated in Figure 15.

4. Discussions

The main difference between incipient rock discontinuities and mechanical ones is that discontinuities at incipient stage have some tensile strength due to rock bridges (Shang et al. 2017b and 2018) or secondary mineralization and cementation (Hoek 2007; Hencher 2012). Given time, they will develop into mechanical fractures in response to loading (Shang et al. 2016), weathering (Goudie 2016) and precipitation (Wieczorek and Jager 1996).

Besides the boundary conditions, Bahaaddini (2017) indicated that the size of gap zone between the upper and lower shear boxes also has some effects on shear mechanism and hence, zero gap zone has been used in this study to reduce the potential effect of gap zone. In this DEM model, incipient rock joints with a particular areal persistence value (0.4) were created, however the potential influence of areal

418 persistence on shear strength will be reported in a separate research paper by the
419 authors. Rock bridges within incipient Horton Formation Siltstone joints were
420 assigned with the same strength to that of adjacent intact rock. Potential weathering
421 and erosion of persistent sections of this lithology, that were observed in the field
422 (Shang et al. 2017b), have not been considered for simplification. Strength
423 weakening can be a potential approach to allow the effect of weathering to be
424 investigated, however, such approach significantly depends on the reliability of input
425 parameters depicting weathering conditions. The strength weakening approach may
426 be evaluated through laboratory tensile and shear tests of weathered rock samples
427 combined with detailed observations in the field.

428 Results of this study show that CNL and CNS boundary conditions had a significant
429 effect on the shear characteristics of incipient rock discontinuities, in terms of peak
430 shear strength (Figure 5), paths of normal stress versus shear stress (Figure 7) and
431 the way of fracturing within rock bridges (Figures 9, 10 and 11). A clear yield
432 behavior was observed in CNS direct shear tests (Figures 5 and 7), which is related
433 to the creation of rupture zones in rock bridges and simultaneously increase of
434 normal stresses.

435 Dilation delineates volumetric expansion of rock materials in deformation
436 (Raziperchikolaee et al., 2014). In this study, smooth-joint model was assigned to the
437 persistent portions with incipient planes to simulate a planar joint surface. Input
438 parameters (Table 1) for this model were calibrated against normal deformability
439 tests (Figure 3b) and direct shear tests (Figure 3c). The DEM model in this study did
440 not consider roughness and asperity. The dilation in the CNS direct shear tests
441 conducted in this study was related to the opening of newly created cracks and
442 generation of the rupture zones within the rock bridges. It should be noted that, in the

particle flow code, dilation can be indirectly simulated by assigning the angle of dilation (Itasca Consulting Group Inc 2008; Raziperchikolaee et al., 2014).

5. Limitations of the study and suggestions for future research

In the calibration of the smooth joint model, the authors failed in their attempts to get reliable data from the direct shear tests under high normal stresses (i.e., 4 and 6 MPa) using the Robertson Shear Box, which is due to its intrinsic limitations when high normal stresses were applied. It was difficult to control the Robertson Shear Box when higher normal stresses were applied (i.e., 4 and 6 MPa) using the equipped hand jack; the applied normal stresses always dropped down and it required continuously manual control by the addition of pressure using the equipped hand jack. These stress alternations have led to errors (human errors may also existed in that procedure). This alternation in normal stress was not observed when a lower normal stress was applied (i.e., 2 MPa). The stress-displacement curve under a normal stress of 2 MPa was therefore used for the calibration of the smooth joint, which is sufficient as a mechanical joint (no true cohesion) was tested. It is suggested that the Golder Shear Box is used in the direct shear tests in the future research. For the Golder Shear Box, a dead weight is used to apply normal stresses, which can eliminate the problems encountered in the study (see Hencher and Richards (2015) for details of the Golder Shear Box).

In addition, it has to be accepted that it is extremely difficult to conduct the physical experiments on natural incipient rock joints. Because natural sample preparation is uncontrollable – it seems impossible to secure a group of incipient rock joints with identical geometrical parameters of rock bridges so that the tests under different boundary conditions are not repeatable. Replica sample may resolve this issue to

some degree but setup of a CNS direct shear test is also extremely difficult. As mentioned in the introduction, the difficulty of experimentation is also one of the reasons that inspired the authors to investigate the CNS shear mechanism using the numerical method. The methodology established in this study provides some insights that allow us to better understand the CNL and CNS shear mechanism, especially at micro-scale level. It is suggested that CNS direct shear tests of natural incipient rock joints are imperative to be conducted in the future to validate the numerical findings in this study.

6. Conclusion

This study presents the shear failure of incipient rock discontinuities under CNL and CNS boundary conditions based on a 3D discrete element method, in which rock matrix and rock bridges were mimicked using discrete rigid particles bonded together at their contacts. Smooth-joint model was assigned to the persistent portions of incipient joint planes. The method allows the creation of incipient rock discontinuities with various areal persistence (that are difficult to obtain through physical models) and the measurement and observation of micro-cracking behavior inside incipient joint planes (which are not currently achievable in the experimentations).

Findings in the study reveal that CNL and CNS boundary conditions had significant effects on the shear characteristics of incipient rock discontinuities. Under CNL boundary conditions, incipient rock joints failed in brittle due to the sudden rupture of rock bridges. Whereas yield behavior occurred for CNS direct shear, which was related to the gradual increase of normal stresses (because of the opening of the newly created fractures and creation of the rupture zones) in the process of shearing, leading to the increase of shear strength. Shear stress increased

significantly with the increase of normal stresses, irrespective of the boundary conditions. Under the same initially applied normal stress, a higher stiffness of confinement resulted in a higher increment of normal stress in CNS direct shear.

It is also found that fracturing behavior depended significantly on the boundary conditions. For the CNL direct shear tested in this study, cracks initiated around rock bridge edges, propagated and coalesced firstly at the middle of the rock bridges. For the CNS shear, however, cracks concentrated around edges first but propagated gradually with an approximately same speed to the middle.

Acknowledgements

Thoughtful discussions with Dr Duan Kang at Nanyang Technological University are thanked. The stereonet software developed by Professor Richard Allmendinger at Cornell University was used to interpret the orientation distribution of the micro-cracks.

References

ASTM D7012, 2014. Standard test method for compressive strength and elastic moduli of intact rock core specimens under varying stages of stress and temperatures. ASTM International, West Conshohocken.

Bahaaddini, M., Sharrock, G., Hebblewhite, B.K., 2013. Numerical direct shear tests to model the shear behaviour of rock joints. Comput. Geotech. 51, 101-115.

Bahaaddini, M., Hagan, P.C., Mitra, R., Khosravi, M.H., 2016. Experimental and numerical study of asperity degradation in the direct shear test. Eng. Geol. 204, 41-52.

513 Bahaaddini, M., 2017. Effect of boundary condition on the shear behaviour of rock
514 joints in the direct shear test. Rock Mech. Rock Eng. DOI 10.1007/s00603-016-
515 1157-z.

516 Bandis, S.C., Lumsden, A.C., Barton, N.R., 1983. Fundamentals of rock joint
517 deformation. Int. J. Rock Mech. Min. Sci. Geomech. Abstr. 20(6), 249-68.

518 Bandis. S., Lumsden, A.C., Barton, N.R.,1981. Scale effects on the shear behavior
519 of rock joints. Int. J. Rock Mech. Min. Sci. Geomech. Abstr. 18, 1–21.

520 Bewick, R.P., Kaiser, P.K., and Bawden, W.F., 2014. Shear rupture under constant
521 normal stiffness boundary conditions. Tectonophysics 634, 76-90.

522 Byerlee, J., 1978. Friction of rocks. Pure Appl. Geophys. 116(4-5)

523 Cundall, P. A., Strack, O. D. L., 1979. A discrete numerical model for granular
524 assemblies. Geotechnique 29(1), 47–65.

525 Cundall, P.A., 2000. Numerical experiments on rough joints in shear using a
526 bonded particle model. In: Aspects of tectonic faulting. Berlin, pp 1-9.

527 Duan, K., Kowk, C.Y., 2016. Evolution of stress-induced borehole breakout in
528 inherently anisotropic rock: Insights from discrete element modelling. J. Geophys.
529 Res. Solid Earth 121, 2361-2381.

530 Einstein, H.H., Veneziano, D., Baecher, G.B., O'Reilly, K.J., 1983. The effect of
531 discontinuity persistence on rock slope stability. Int. J. Rock Mech. Min. Sci, 20(5),
532 227-236.

533 Fairhurst, C.E, Hudson, J.A., 1999. Draft ISRM suggested method for the complete
534 stress-strain curve for intact rock in uniaxial compression. Int. J. Rock Mech. Min.
535 Sci, 36(3), 281-289.

536 Gehle, C., Kutter, H.K., 2003. Breakage and shear behavior of intermittent rock
537 joints. Int. J. Rock Mech. Min. Sci. 40, 687-700.

538 Gischig, V. S., Amann, F., Moore, J.R., Loew, S., Eisenbeiss, H., Stempfhuber, W.,
539 2011. Composite rock slope kinematics at the current Randa instability,
540 Switzerland, based on remote sensing and numerical modelling. Eng. Geol. 118,
541 37-53.

542 Gischig, V.S., Moore, J.R., Evans, K.F., Amann, F., Loew, S., 2011a.
543 Thermomechanical forcing of deep rock slope deformation: 1. Conceptual study of
544 a simplified slope. J. Geophs. Res. 116, 1-18.

545 Gischig, V.S., Moore, J.R., Evans, K.F., Amann, F., Loew, S., 2011b.

546 Thermomechanical forcing of deep rock slope deformation: 2. The Randa

547 rock slope in stability. J. Geophys. Res. doi:10.1029/2011JF002007

548 Goudie, A.S., 2016. Quantification of rock control in geomorphology. Earth-Sci.,
549 Rev. 159, 374-387.

550 Hencher, S.R., 1976. A simple sliding apparatus for the measurement of rock
551 friction. Geotechnique 26(4), 641–644.

552 Hencher, S.R., Lee, S.G., Carter, T.G., Richards, L.R., 2011. Sheet joints:
553 characterization, shear strength and engineering. Rock Mech. Rock. Eng. 44, 1-22.

554 Hencher, S.R., 2012. Practical engineering geology. Spon Prress, Talyor & Francis,
555 Oxon.

556 Hencher, S.R., Richards, L.R., 2015. Assessing the shearing strength of rock
557 discontinuities at laboratory and field scales. Rock Mech. Rock Eng. 48, 883-905.

558 Hoek, E., 2007. Practical rock engineering. pp 342, https://www.rocscience.com.

559 Indraratna, B., Haque, A., 2000. Experimental and numerical modeling of shear
560 behaviour of rock joints. GeoEng 2000, An International Conference on
561 Geotechnical & Geological Engineering, 1, Invited Papers Pennsylvania, USA:
562 Technomic Publishing Co Inc.

563 Indraratna, B., Haque, A., 2000. Shear behaviour of rock joints. University of
564 Wollongong, Australia.

565 Indraratna, B., Haque, A., 1997. Experimental study of shear behaviour of rock
566 joints under constant normal stiffness conditions. Int. J. Rock Mech. Min. Sci &
567 Geomech. Abstr. 34(3-4), 534-541.

568 Itasca Consulting Group Inc, 2008. PFC3D manual, version 4.0. Minneapolis,
569 Minnesota

570 Karami, A., Greer, S., Beddoes, R., 2007. Numerical assessment of step-path
571 failure of northwest wall of A154 Pit, Diavik Diamond Mines. In: Potvin, Y. (Ed.),
572 Proceedings of the 2007 International Symposium on Rock Slope Stability in Open
573 Pit Mining and Civil Engineering. CSIRO, Perth, Australia, 293-305.

574 Kemeny, J., 2005. Time-dependent drift degradation due to the progressive failure
575 of rock bridges along discontinuities. Int. J. Rock Mech. Min. Sci. 42, 35-46.

576 Kim, H.M., Inoue, J., 2003. Analytical approach for anisotropic permeability through
577 a single rough rock joint under shear deformation. J. Geophys. Res. 108(B8), 2366,
578 doi:10.1029/2002JB002283.

579 Lajtai, E.Z., 1969. Strength of discontinuous rocks in direct shear. Geotechnique
580 19(2), 28-233.

581 Lee, Y.K., Park, J.W., Song, J.J., 2014. Model for the shear behaviour of rock joints
582 under CNL and CNS conditions. Int. J. Rock Mech. Min. Sci. 70, 252-263.

583 Mehranpour, M.H., Kulatilake, P.H.S.W., 2017. Improvements for the smooth joint
584 contact model of the particle flow code and its applications. Comput. Geotech. 87,
585 163-177.

586 Nemcik, J., Ma, S.Q., Aziz, N., Ren, T., Geng, X., 2014. Numerical modelling of
587 failure propagation in fully grouted rock bolts when subjected to tensile load. Int. J.
588 Rock Mech. Min. Sci. 71, 293-300.

589 Poturovic, S., Schubert, W., Blumel, M., 2015. Comparison of constant normal load
590 and constant normal stiffness (CNS) direct shear tests. In: Eurock 2015 & 64th
591 Geomechanics Colloquium, Salzburg, Austria.

592 Potyondy, D.O., Cundall, P.A., 2004. A bonded-particle model for rock. Int. J. Rock
593 Mech. Min. Sci. 41: 1329-1364.

594 Raziperchikolaee, S., Alvarado, V., Yin, S., 2014. Effect of fracture roughness on
595 seismic source and fluid transport responses. Gephys. Res. Lett. 41, 1530-1536.

596 Saeb, S., Amadei, B.,1990. Modelling joint response under constant or variable
597 normal stiffness boundary conditions. Int. J. Rock Mech. Min. Sci & Geomech.
598 Abstr. 27(3), 213-217.

599 Savilahti, T., Nordlund, E., Stephansson, O., 1990. Shear box testing and modeling
600 of joint bridge. In: Proceedings of international symposium on shear box testing and
601 modeling of joint bridge Rock Joints, Norway, 295–300.

602 Shang, J., Hencher, S.R., West, L.J., 2015. Tensile strength of incipient rock
603 discontinuities. In: Eurock 2015 & 64th Geomechanics Colloquium, Salzburg,
604 Austria.

605 Shang, J., 2016. Persistence and tensile strength of incipient rock discontinuities.
606 PhD thesis, the University of Leeds. Leeds, United Kingdom, 248p

607 Shang, J., Duan, K., Gui, Y., Handley, K., Zhao, Z., 2017a. Numerical investigation
608 of the direct tensile behaviour of laminated and transversely isotropic rocks
609 containing incipient bedding planes with different strengths. Comput. Geotech. Doi:
610 Comput. Geotech., doi: https://doi.org/10.1016/j.compgeo.2017.11.007.

611 Shang, J., Hencher, S.R., West, L.J., 2016. Tensile strength of geological
612 discontinuities including incipient bedding, rock joints and mineral veins. Rock
613 Mech. Rock Eng., 49(11) 4213-4225.

614 Shang, J., Hencher, S.R., West, L.J., Handley, K., 2017b. Forensic excavation of
615 rock masses: A technique to investigate discontinuity persistence. Rock Mech.
616 Rock Eng., doi: 10.1007/s00603-017-1290-3.

617 Shang, J., West, L.J., Hencher, S.R., Zhao, Z., 2018. Tensile strength of large-scale
618 incipient rock joints: a laboratory investigation. Acta Geotech., doi: 10.1007/s11440-
619 017-0620-7 .

620 Shrivastava, A.K., Rao, K.S., 2013. Development of a large-scale direct shear
621 testing machine for unfilled and infilled rock joints under constant normal stiffness
622 conditions. Geotech. Test. J. 36(5), 670-679.

623 Shrivastava, A.K., Rao, K.S., 2010. Numerical simulation of direct test for rock. In:
624 Indian Geotechnical Conference, IGS Mumbai Chapter & IIT Bombay.

625 Stead, D., Wolter, A., 2015. A critical review of rock slope failure mechanisms: the
626 importance of structural geology. J. Struct. Geol. 74, 1-23.

627 Tannant, D.D., Giordan, D., Morgenroth, J., 2017. Characterization and analysis of
628 a translational rockslide on a stepped-planar slip surface. Eng. Geol. 220(30), 144-
629 151.

630 Thirukumaran, S., Indraratna, B., 2016. A review of shear strength models for rock
631 joints subjected to constant normal stiffness. J. Rock Mech. Geotech. Eng. 8, 405-
632 414.

633 Tuckey, Z., Stead, D., 2016. Improvements to field and remote sensing methods for
634 mapping discontinuity persistence and intact rock bridges in rock slopes. Eng Geol.
635 208, 136-153.

636 Wieczorek, G.F., Jager, S., 1996. Triggering mechanisms and depositional rates of
637 postglacial slope-movement processes in the Yosemite Valley, California.
638 Geomorphology 15, 17-31.

639 Zhang, H.Q., Zhao, Z.Y., Tang, C.A. Song. L., 2006. Numerical study of shear
640 behaviour of intermittent rock joints with different geometrical parameters. Int. J.
641 Rock Mech. Min. Sci. 43, 802-816.

642 Zhang, L., and Thornton, C., 2007. A numerical examination of the direct shear test,
643 Geotechnique 57(4), 343-354.

644 **Figure captions**

645 **Figure 1.** A rock slope adjacent to a highway in Taiwan showing massive blocks.
646 Adapted from Shang et al. 2016.

647 **Figure 2.** Schematic diagram showing CNL and CNS boundary conditions.

648 **Figure 3.** DEM model calibration against characteristics of Horton Formation
649 Siltstone. Results from laboratory experiment and the DEM model: (a) Uniaxial
650 compressive strength of intact rock; (b) Normal deformability test results and (c)
651 direct shear strength of planar Horton Formation Siltstone joints.

652 **Figure 4.** Model setup under CNL ((a) and (c)) and CNS ((b) and (d)) boundary
653 conditions.

654 **Figure 5.** Shear stress against shear strain of an incipient rock joint under CNL and
655 CNS boundary conditions under normal stresses of (a) 6 MPa, (b) 20 MPa and (c) 40
656 MPa.

657 **Figure 6.** Relative increase of yield and peak stresses against initially applied normal
658 stresses in CNS direct shear.

659 **Figure 7.** Shear stress plotted against normal stress for CNS direct shear under
660 initially applied normal stresses of (a) 6 MPa, (b) 20 MPa and (c) 40 MPa.

Figure 8. Peak normal stress versus cap modulus under CNS direct shear. CNL direct shear occurred when cap modulus equals to zero.

Figure 9. CNL shear characteristics at a normal stress of 6 MPa. (a) Measured shear stress against shear strain; (b) Normal displacement versus shear strain; (c) Cumulative number of total, shear and tensile cracks versus horizontal shear displacement/strain and (d) monitored development of micro-cracks. Red discs donate shear cracks and yellow discs tensile cracks.

Figure 10. CNS shear characteristics at initially applied normal stress of 6 MPa and cap modulus of 1 GPa. (a) and (b) Monitored shear stress vs. strain using measured spheres shown in Figure 4d; (c) Normal stress against shear strain; (d) cumulative number of cracks versus horizontal displacement/strain and (e) Development of micro-cracks.

Figure 11. CNS shear characteristics at initially applied normal stress of 6 MPa and cap modulus of 30 GPa. (a) and (b) Monitored shear stress vs. strain using measured spheres shown in Figure 4d; (c) Normal stress against shear strain; (d) Cumulative number of cracks versus horizontal displacement/strain and (e) development of micro-cracks.

Figure 12. Orientation of cracks in CNL direct shear test (first row) and CNS direst shear test (rest of rows), where both the normal stress (for CNL shear) and initially applied normal stress (for CNS shear) are 6 MPa.

Figure 13. Orientation of cracks in CNL direct shear test (first row) and CNS direst shear test (rest of rows), where both the normal stress (for CNL shear) and initially applied normal stress (for CNS shear) are 20 MPa.

Figure 14. Orientation of cracks in CNL direct shear test (first row) and CNS direst shear test (rest of rows), where both the normal stress (for CNL shear) and initially applied normal stress (for CNS shear) are 40 MPa.

Figure 15. Number of induced micro-cracks against peak normal stress in CNL and CNS direct shear.

Table caption

Table 1 Input micro-parameters of particles, bonds and smooth joints for the DEM model.

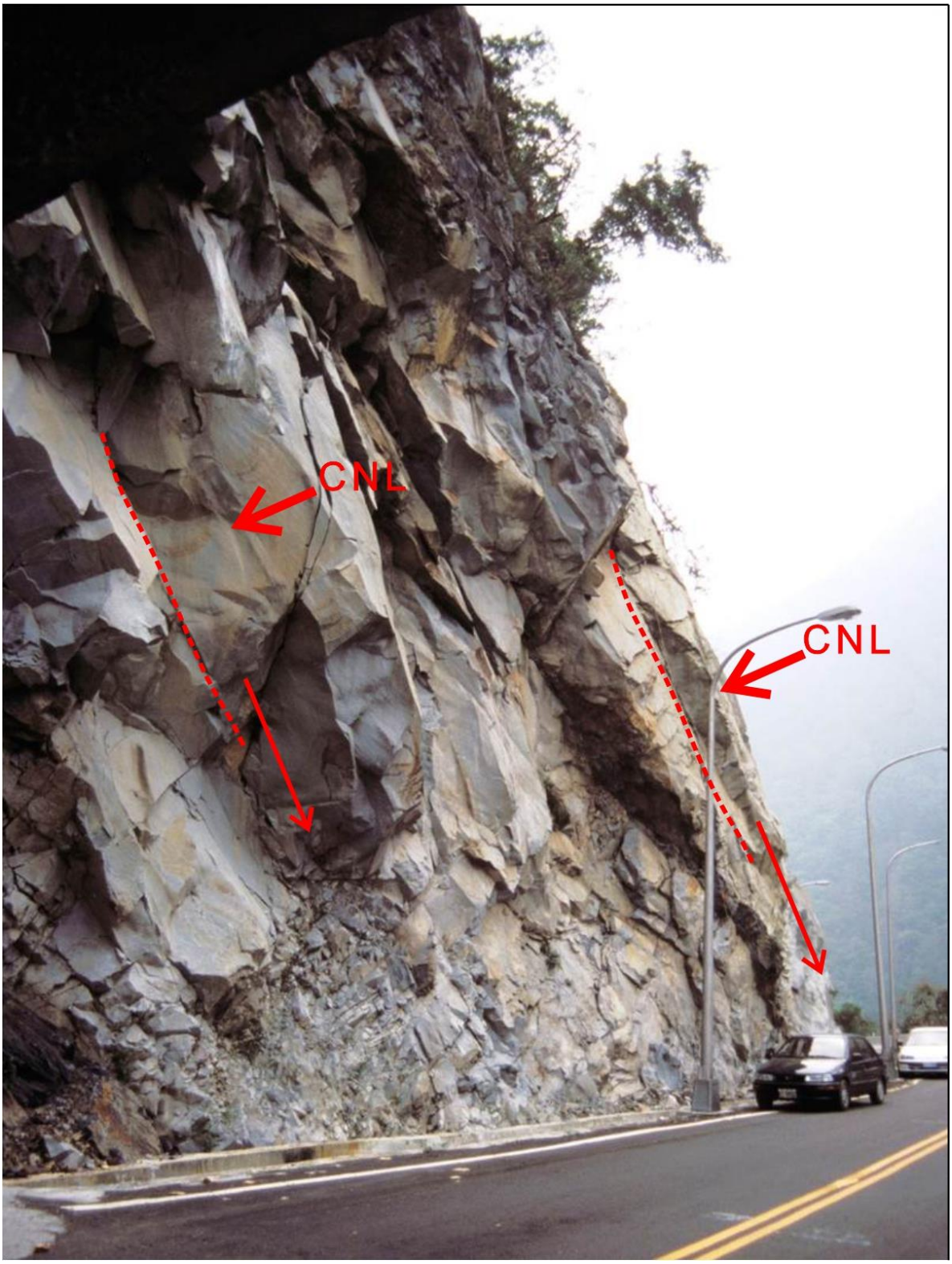

Fig 1

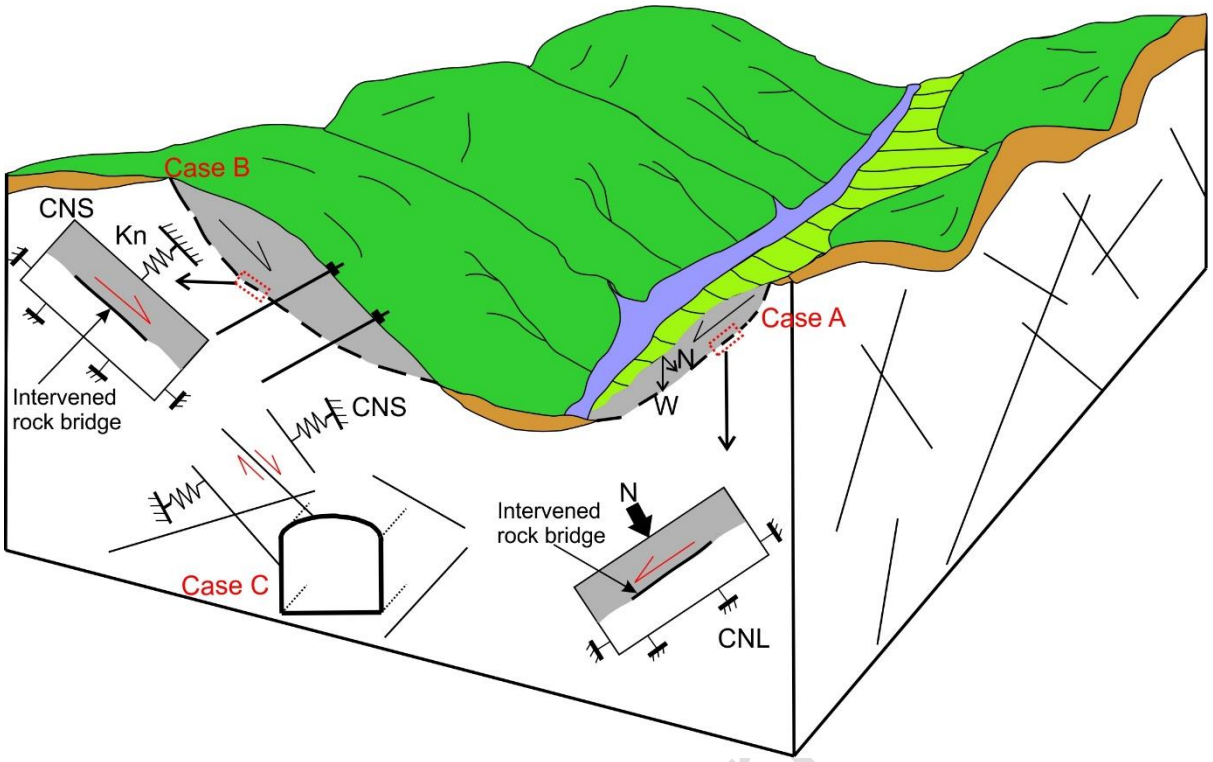

707

708 **Fig 2**

709

710

711

712

713

714

715

716

717

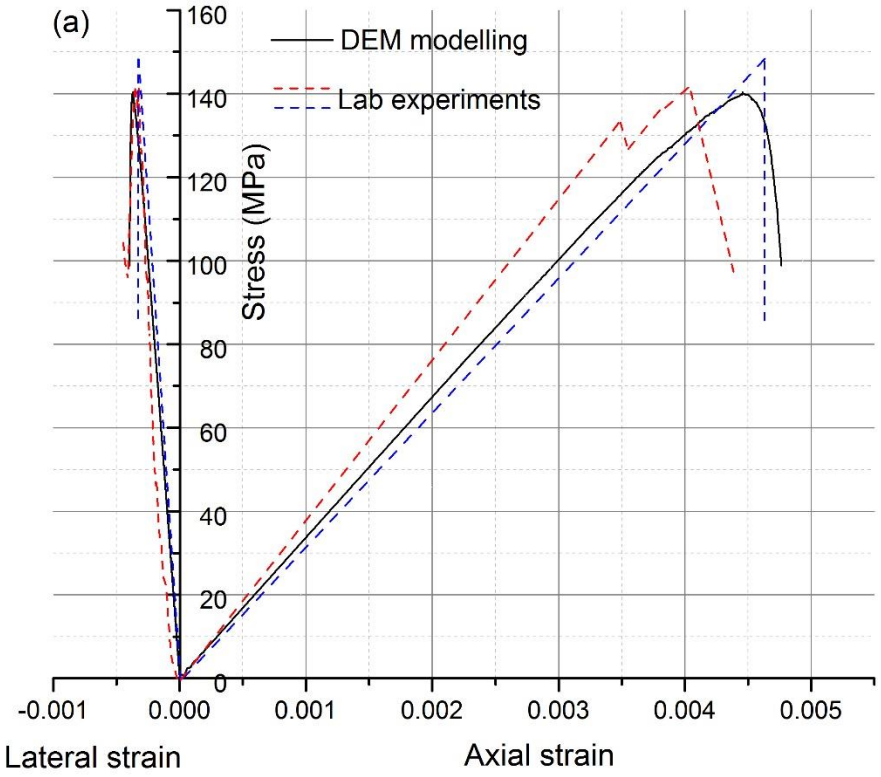

718

719 **Fig 3a**

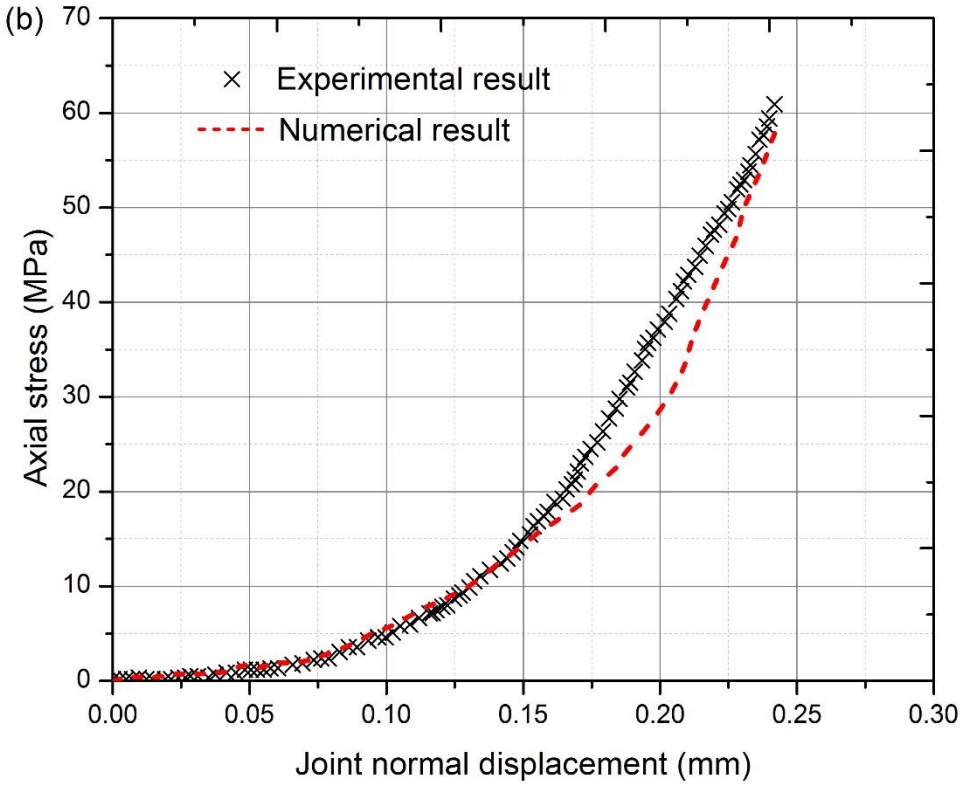

720

721 **Fig 3b**

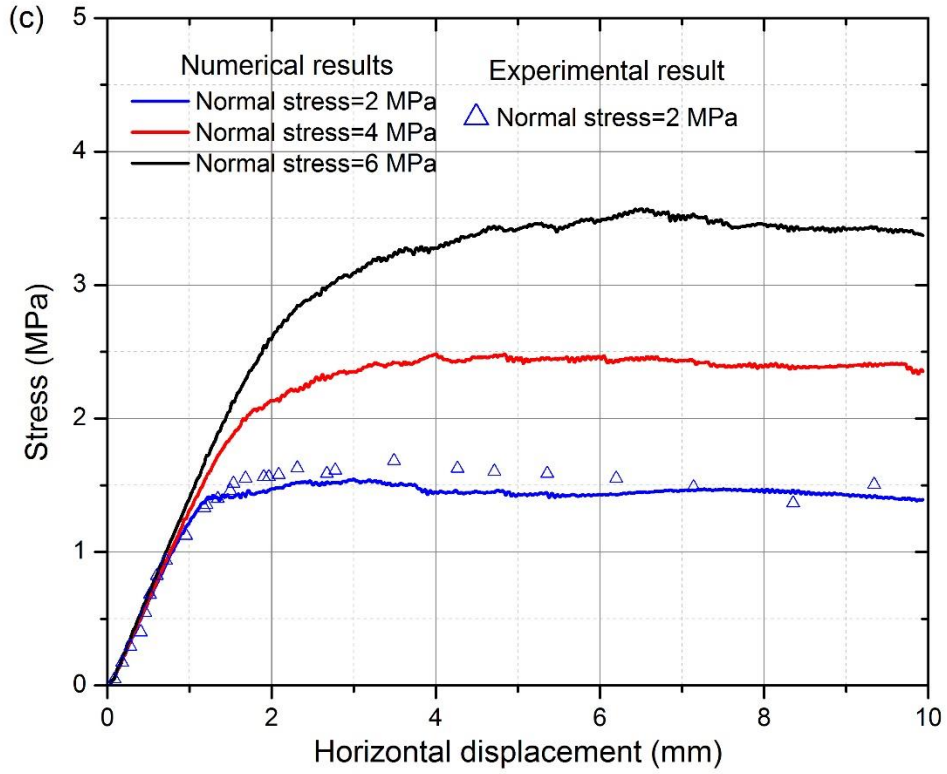

722

723 **Fig 3c**

724
725
726
727
728
729

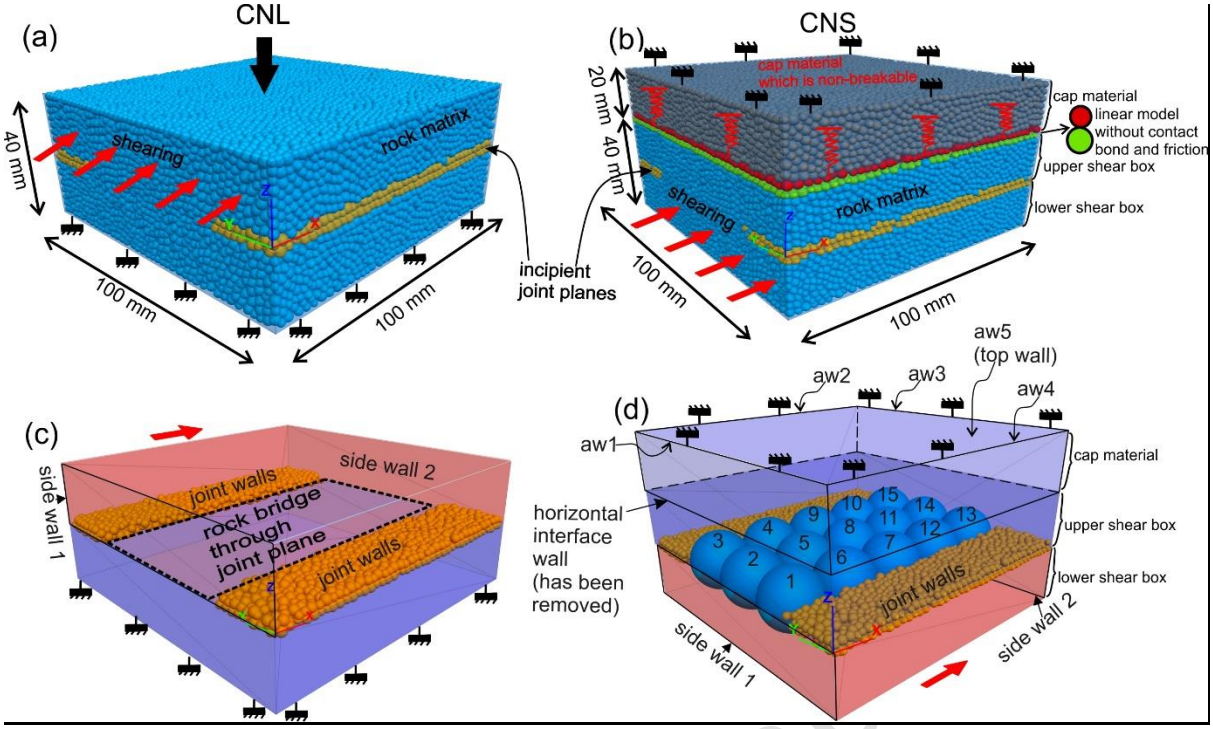

730

731 **Fig 4**

732

733

734

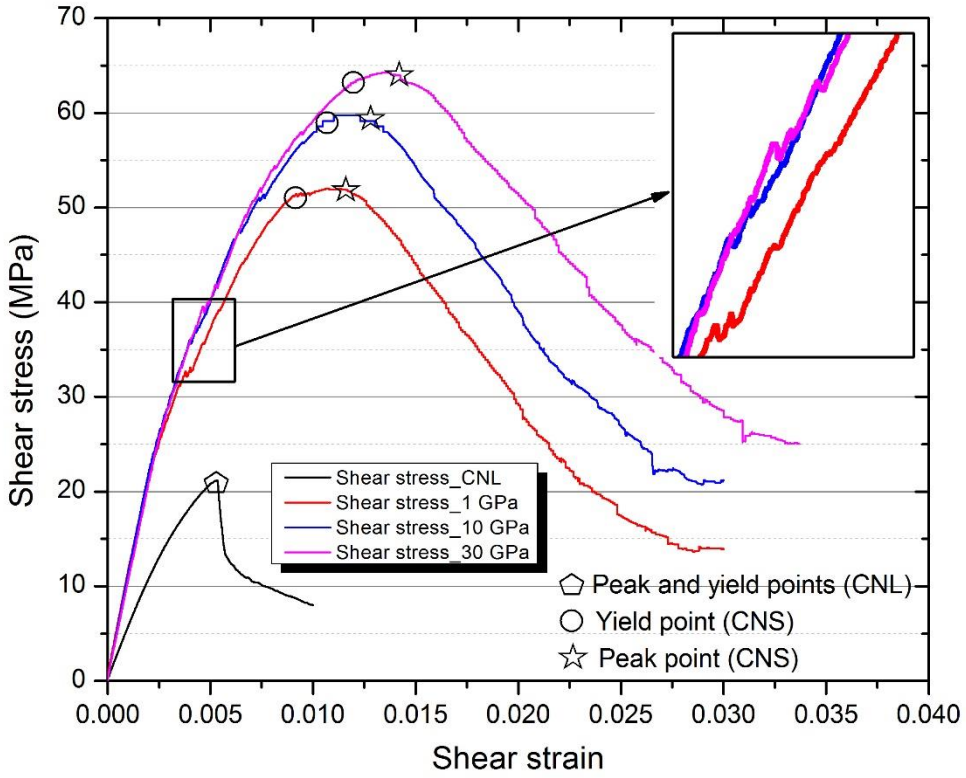

735

736 **Fig 5a**

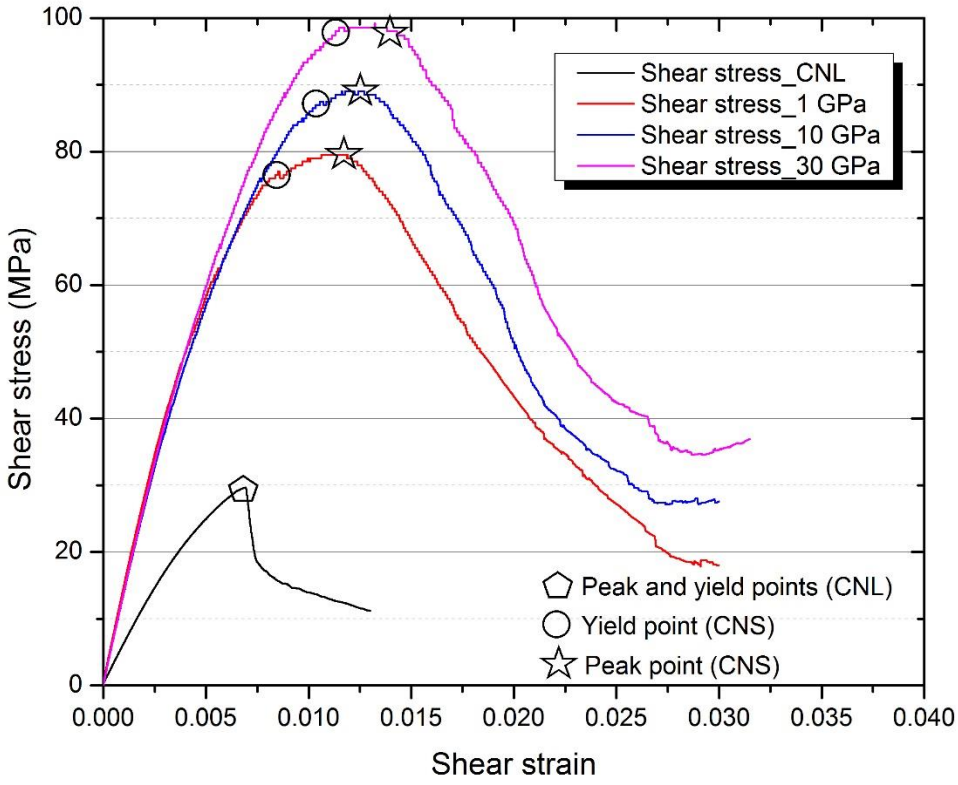

737

738 **Fig 5b**

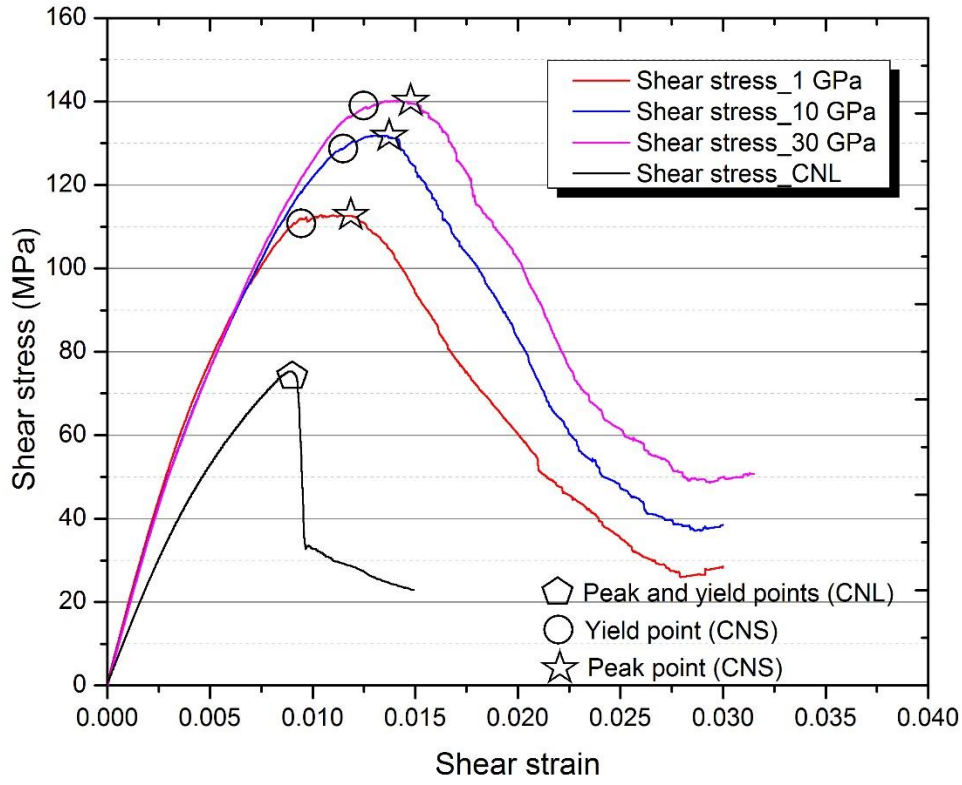

739

740 **Fig 5c**

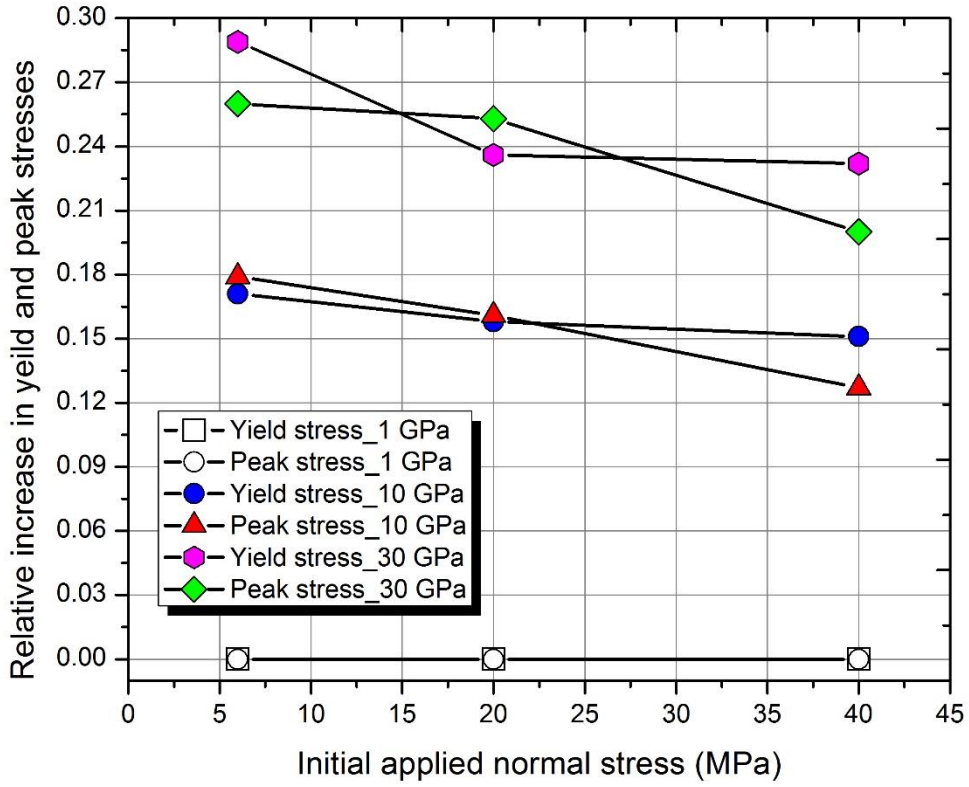

741

742 **Fig 6**

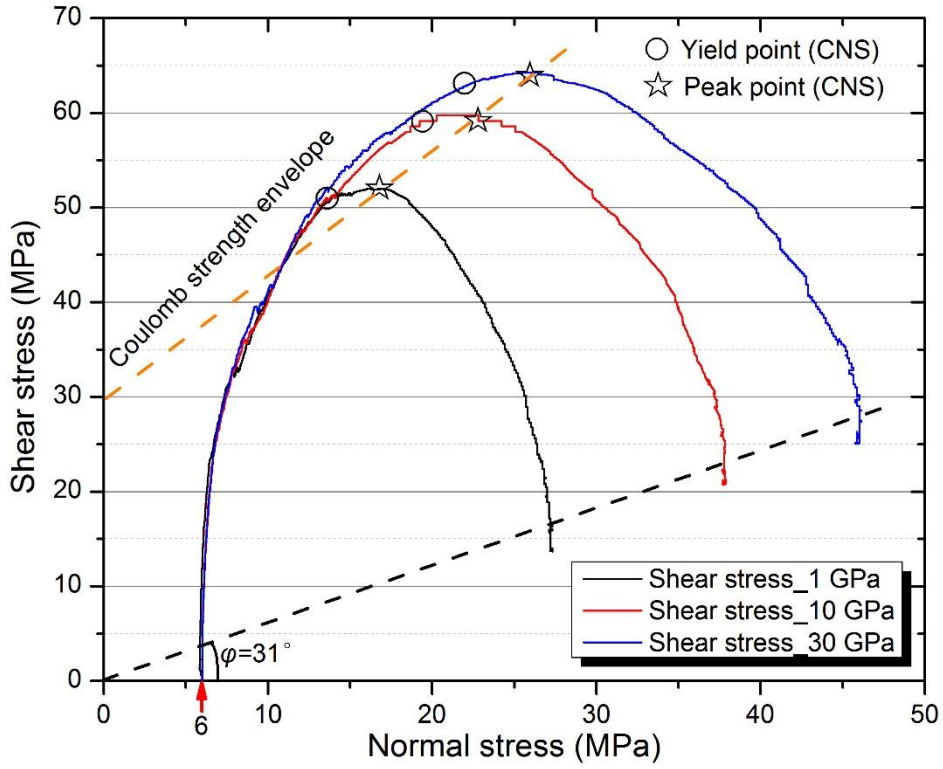

743

744 **Fig 7a**

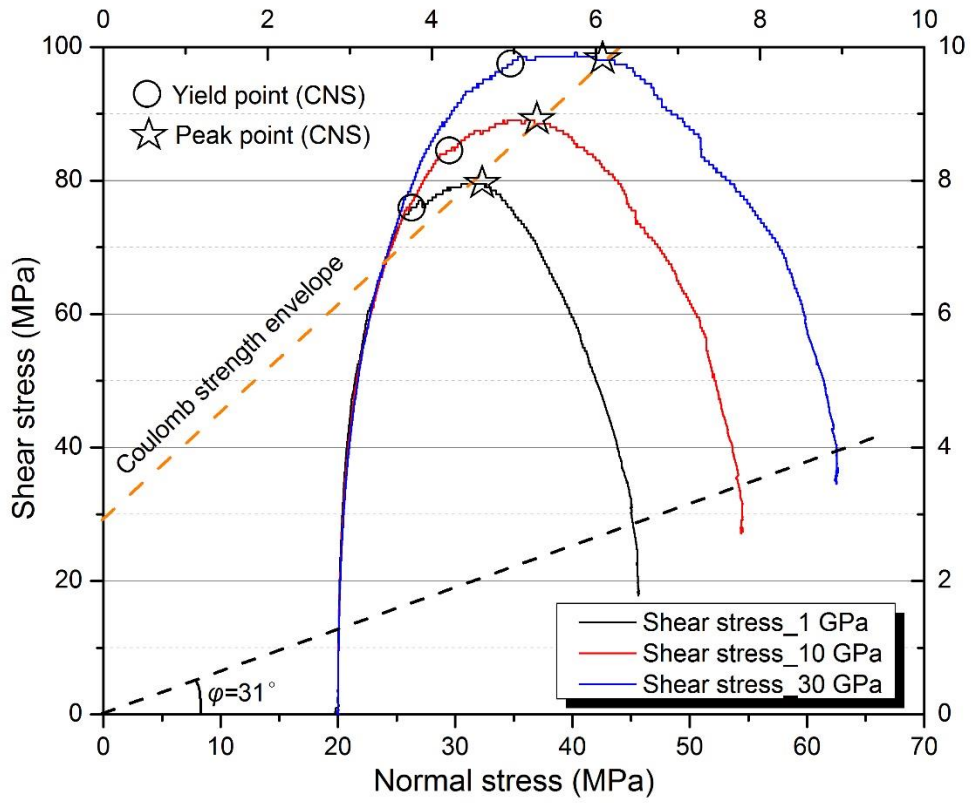

745

746 **Fig 7b**

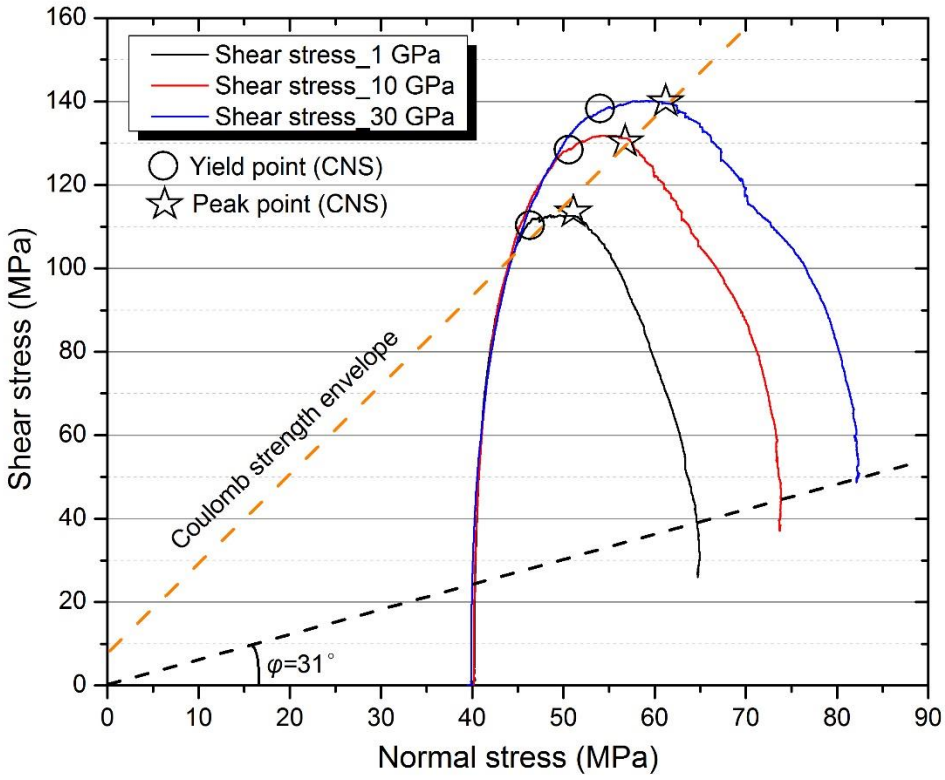

747

748 **Fig 7c**

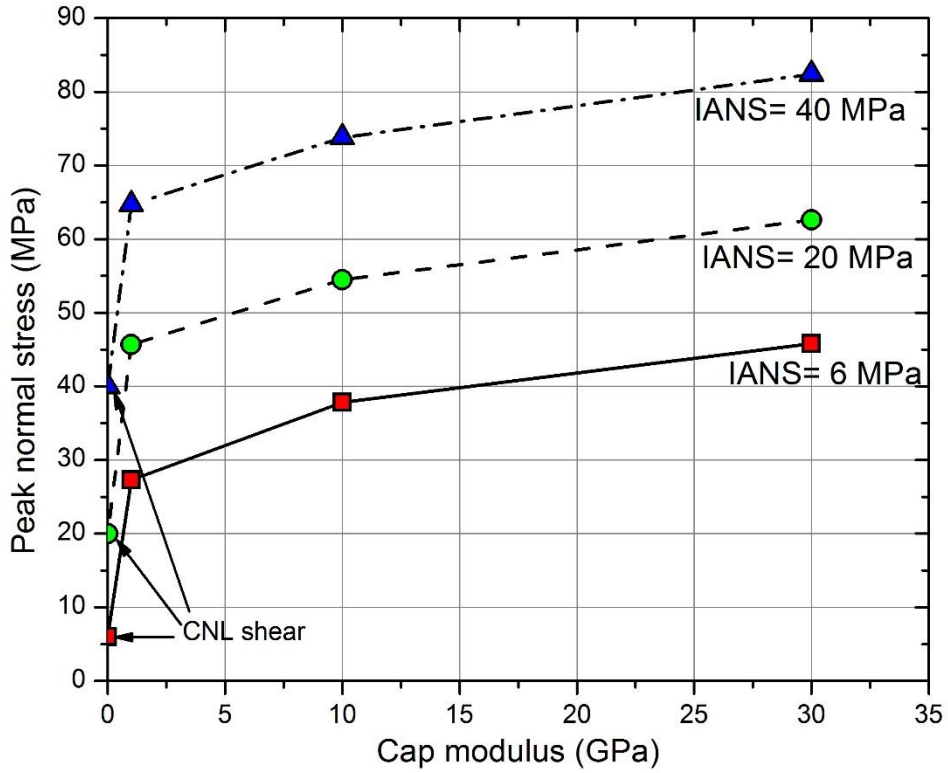

749

750 **Fig 8**

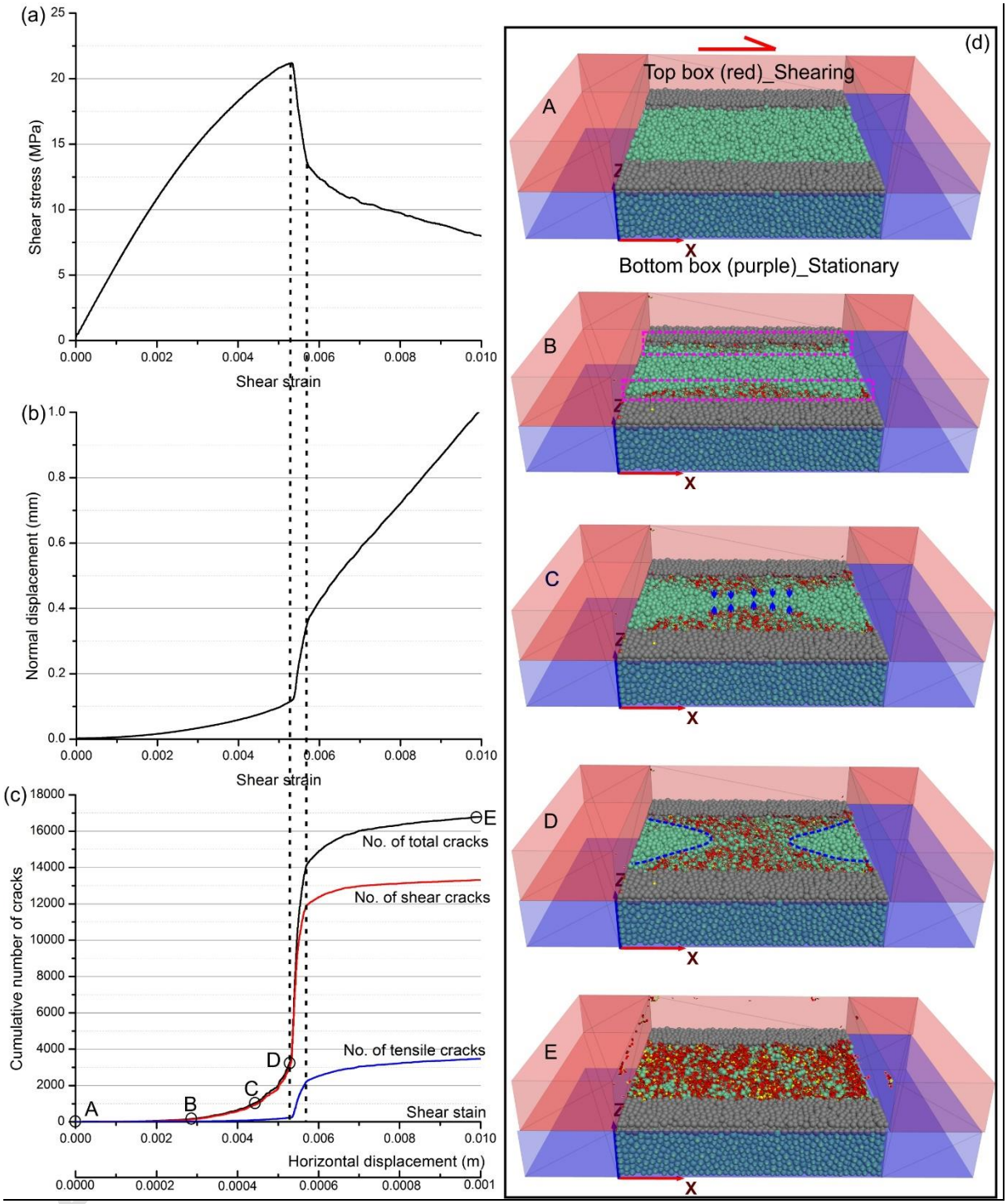
(a)
Shear stress (MPa)
Shear strain
(b)
Normal displacement (mm)
Shear strain
(c)
Cumulative number of cracks
No. of total cracks
No. of shear cracks
No. of tensile cracks
Shear stain
Horizontal displacement (m)
A
B
C
D
E
(d)
Top box (red)_Shearing
Bottom box (purple)_Stationary
Z
X

751

752 **Fig 8**

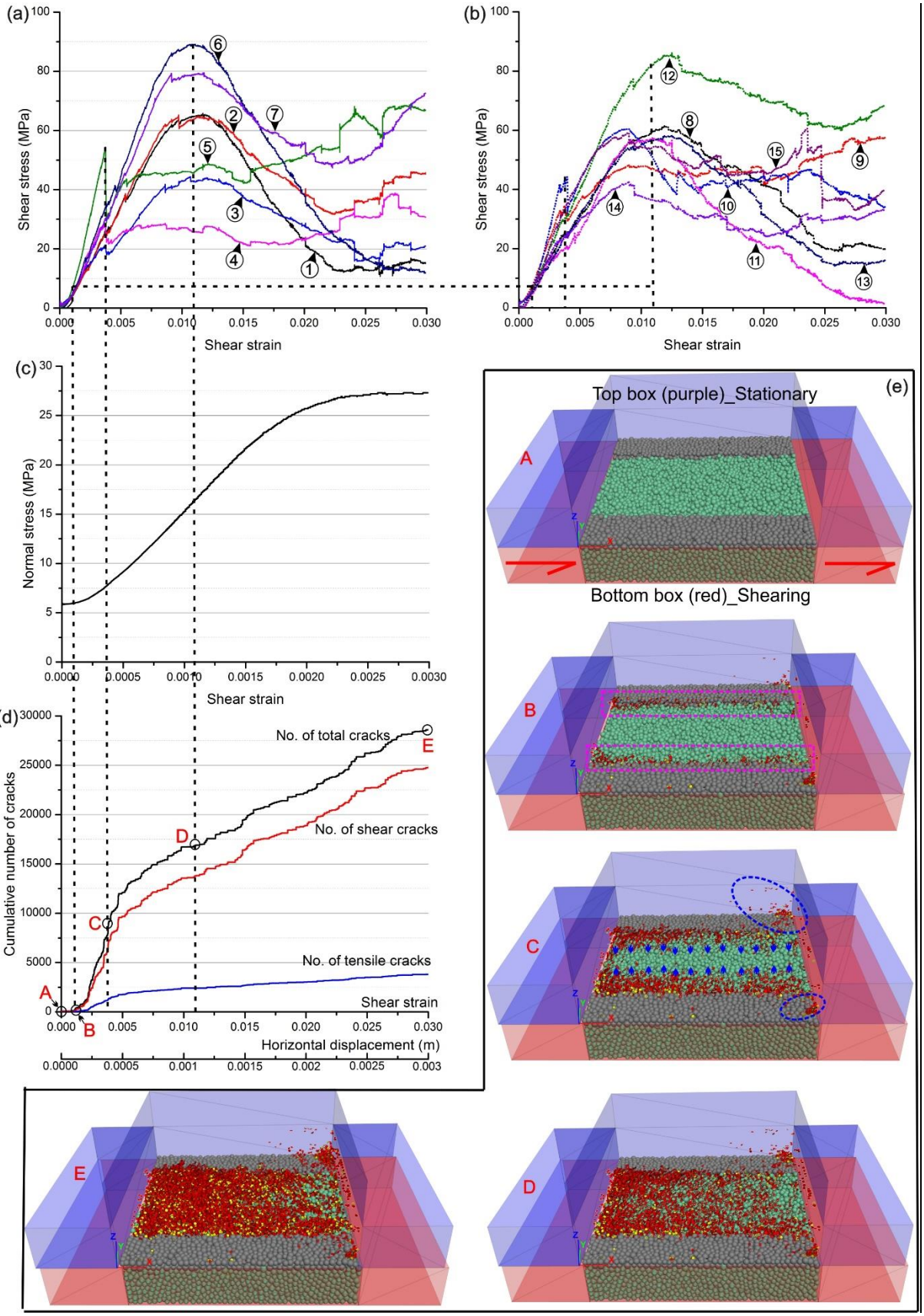
(a)
Shear stress (MPa)
Shear strain
(b)
Shear stress (MPa)
Shear strain
(c)
Normal stress (MPa)
Shear strain
(d)
Cumulative number of cracks
No. of total cracks
No. of shear cracks
No. of tensile cracks
Shear strain
Horizontal displacement (m)
A
B
C
D
E
(e)
Top box (purple)_Stationary
Bottom box (red)_Shearing

753

754 **Fig 9**

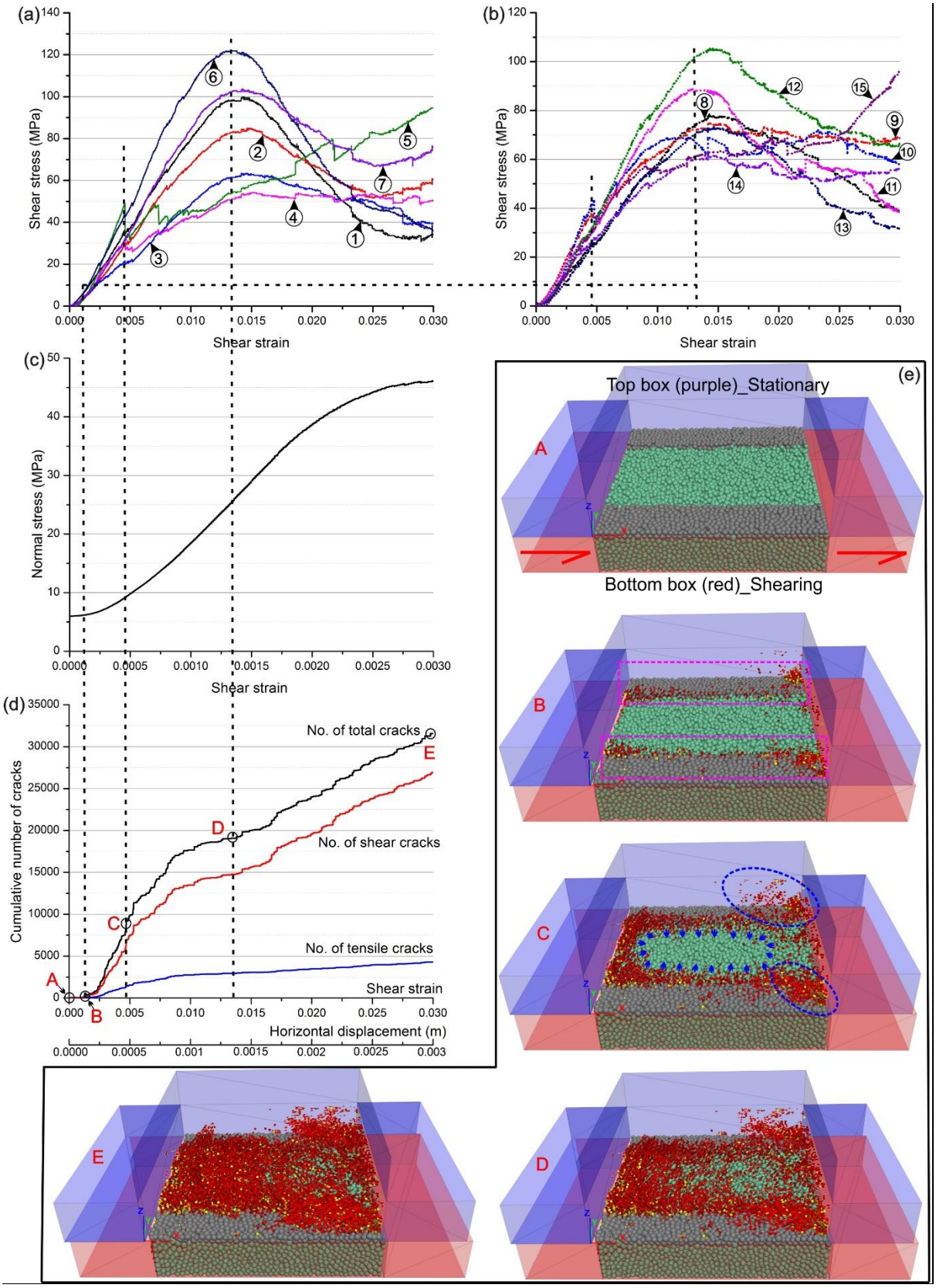
(a)
Shear stress (MPa)
Shear strain
(b)
Shear stress (MPa)
Shear strain
(c)
Normal stress (MPa)
Shear strain
(d)
Cumulative number of cracks
No. of total cracks
No. of shear cracks
No. of tensile cracks
Shear strain
Horizontal displacement (m)
A
B
C
D
E
(e)
Top box (purple)_Stationary
Bottom box (red)_Shearing

Fig 10

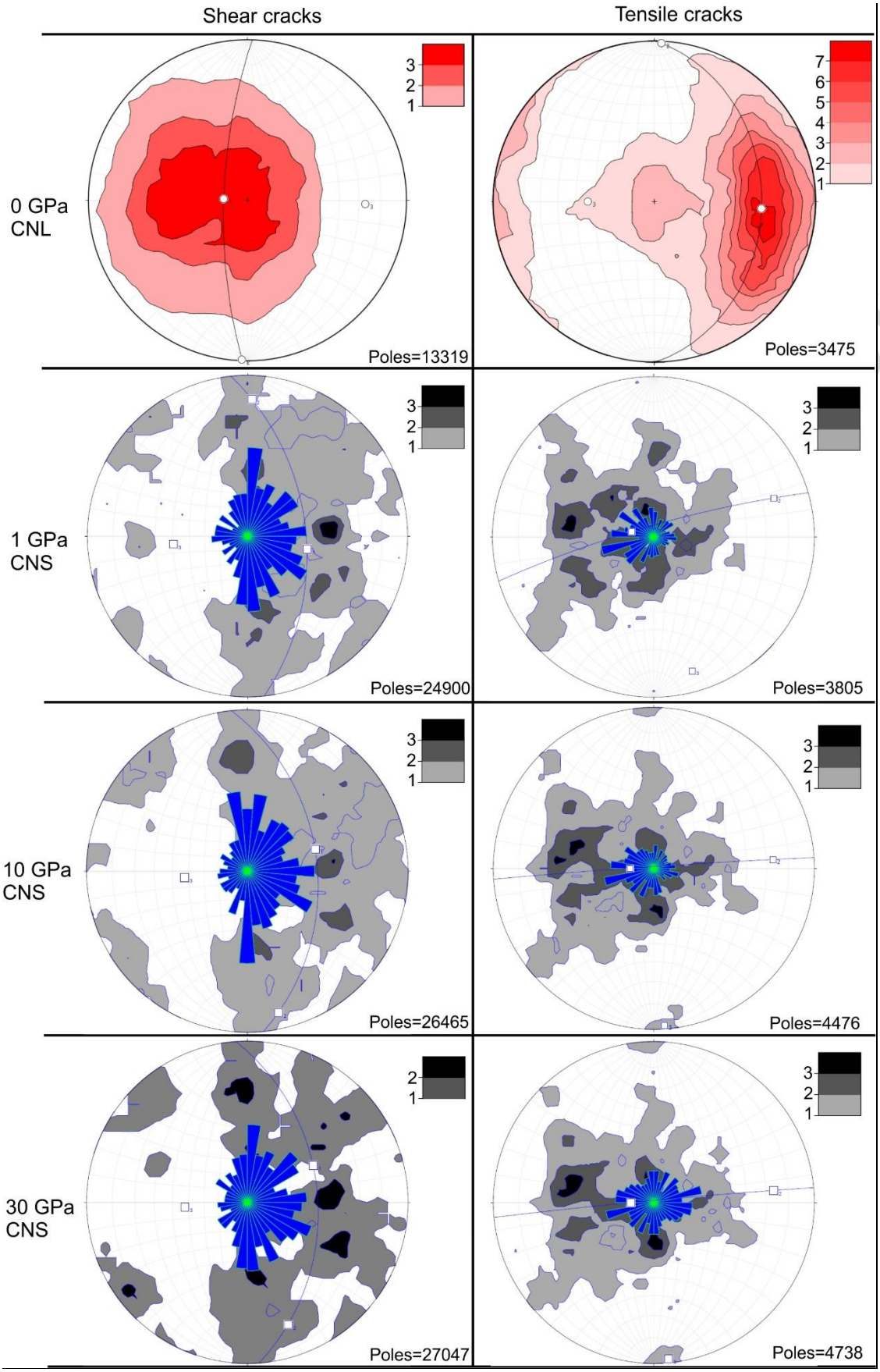
Shear cracks
Tensile cracks
0 GPa
CNL
1 GPa
CNS
10 GPa
CNS
30 GPa
CNS
Poles=13319
Poles=3475
Poles=24900
Poles=3805
Poles=26465
Poles=4476
Poles=27047
Poles=4738

757

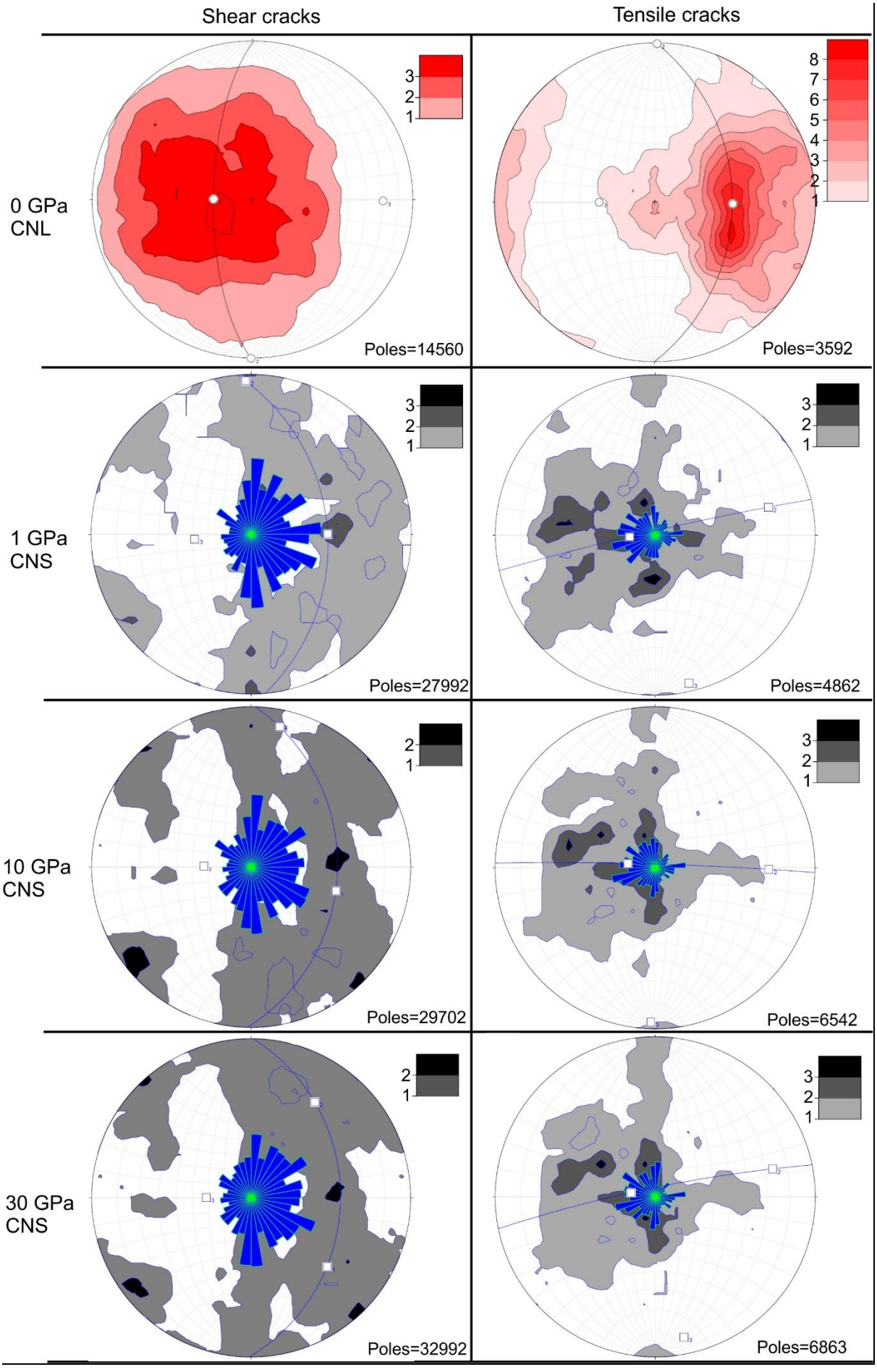
Shear cracks
Tensile cracks
0 GPa
CNL
Poles=14560
Poles=3592
1 GPa
CNS
Poles=27992
Poles=4862
10 GPa
CNS
Poles=29702
Poles=6542
30 GPa
CNS
Poles=32992
Poles=6863

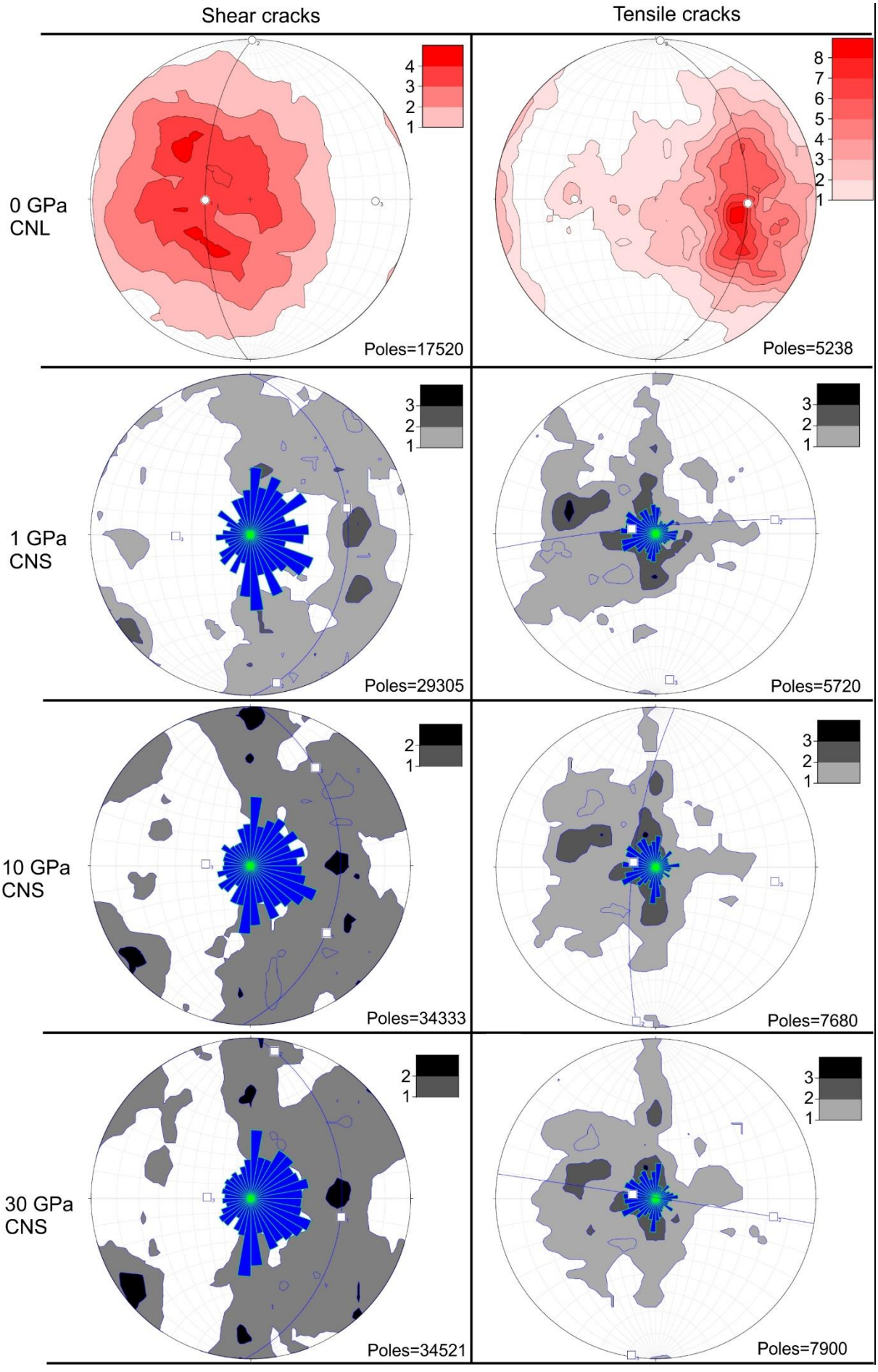
Shear cracks
Tensile cracks
0 GPa
CNL
Poles=17520
Poles=5238
1 GPa
CNS
Poles=29305
Poles=5720
10 GPa
CNS
Poles=34333
Poles=7680
30 GPa
CNS
Poles=34521
Poles=7900

759

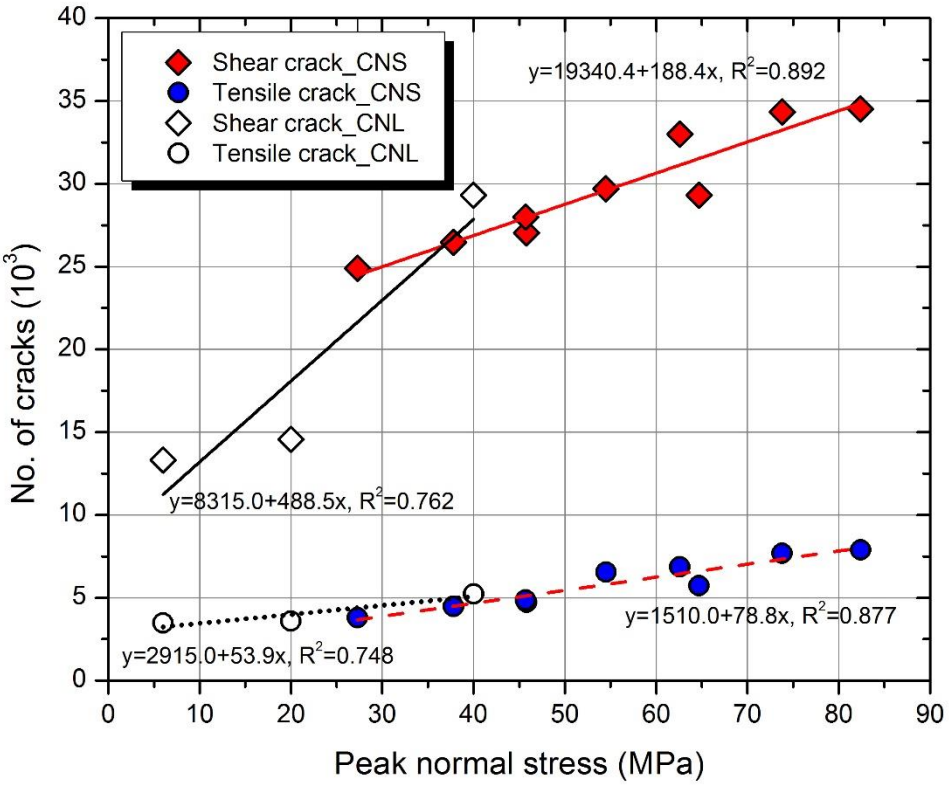

760